A priori control of zeolite phase competition and intergrowth with high-throughput simulations

Daniel Schwalbe-Koda[1], Soonhyoung Kwon[2], Cecilia Paris[3], Estefania Bello-Jurado[3], Zach Jensen[1], Elsa Olivetti[1], Tom Willhammar[4], Avelino Corma[3], Yuriy Román-Leshkov[2], Manuel Moliner[3,*], Rafael Gómez-Bombarelli[1,*]

Affiliations:

[1]Department of Materials Science and Engineering, Massachusetts Institute of Technology, Cambridge, MA 02139.

[2]Department of Chemical Engineering, Massachusetts Institute of Technology, Cambridge, MA 02139.

[3]Instituto de Tecnología Química, Universitat Politècnica de València-Consejo Superior de Investigaciones Científicas, Avenida de los Naranjos s/n, 46022 Valencia, Spain.

[4]Department of Materials and Environmental Chemistry, Stockholm University, Stockholm, SE-106 91, Sweden.

[*]Correspondence to: mmoliner@itq.upv.es, rafagb@mit.edu

Abstract

Zeolites are versatile catalysts and molecular sieves with large topological diversity, but managing phase competition in zeolite synthesis is an empirical, labor-intensive task. Here, we controlled phase selectivity in templated zeolite synthesis from first principles by combining high-throughput atomistic simulations, literature mining, human-computer interaction, synthesis, and characterization. Proposed binding metrics distilled from over 586,000 zeolite-molecule simulations reproduced the extracted literature and rationalize framework competition in the design of organic structure-directing agents. Energetic, geometric, and electrostatic descriptors of template molecules were found to regulate synthetic accessibility windows and aluminum distributions in pure-phase zeolites. Furthermore, these parameters allowed realizing an intergrowth zeolite through a single bi-selective template. The computation-first approach enabled controlling both zeolite synthesis and structure composition using *a priori* theoretical descriptors.

One Sentence Summary

Theory and computation enabled *a priori* selectivity control in zeolite synthesis.

Main Text

Zeolites are nanoporous materials with wide applications in industrial and sustainable catalysis and separations (*1*, *2*). Although topological diversity makes zeolites versatile, this diversity stems from phase competition between metastable polymorphs, which hinders rational design of new synthesis routes for zeolites (*3*–*5*). Computer simulations can guide experimental work by predicting the affinity between organic structure-directing agents (OSDAs) and targeted topologies (*6*–*8*). Recent studies adopted this strategy by simulating up to thousands of OSDAs for a few frameworks at a time (*8*–*10*), but cannot predict whether the proposed OSDAs are more favorable toward another zeolite rather than the desired ones. Accordingly, relatively few experimental realizations have been reported from such studies, as computer-designed OSDA candidates often fail to crystallize the targeted structures. In addition, design algorithms usually lead to molecules with low synthetic accessibility (*6*, *11*). Manual literature analysis can inform heuristics for zeolite synthesis and avoid expensive simulations (*12*), but datasets compiled from tens of papers are limited in their ability to explain phase selectivity in combinatorial host-guest pairings and have only been attempted for template-free synthesis routes. Finally, although several databases of experimental and hypothetical zeolite structures exist (*13*–*15*), few datasets containing OSDAs or OSDA-zeolite affinities are publicly available. A general approach to simultaneously rationalize phase competition of zeolites, retroactively validate synthesis routes from the literature, control the trade-off between OSDA selectivity and synthetic complexity, and tailor the heteroatom distribution of the targeted materials has not yet been realized. Here, we simulated over half a million zeolite-OSDA pairs, proposed design principles that outperformed traditional binding energy metrics in reproducing synthesis outcomes from more than one thousand papers, and demonstrated the phase-selective synthesis of targeted zeolites from newly identified OSDAs. The computational approach allowed the synthesis of SSZ-39 (**AEI**) and SSZ-13 (**CHA**) zeolites under a wide range of conditions, relating broader synthetic accessibility windows to binding and geometric descriptors of templates. Furthermore, fine-tuning the charge distribution of OSDAs modulated the aluminum pairing in zeolites, as demonstrated for the **CHA** framework. Finally, the design toolkit also enabled synthesizing an aluminosilicate **CHA**/**AEI** intergrowth from a single OSDA, showcasing opportunities for tuning catalytic properties by controlling zeolite phase competition. The integrated platform from this work is made available for the public (see Data Availability) and is expected to drastically accelerate the design and optimization of zeolites.

Phase competition and literature data

To capture phase competition with atomistic simulations, we postulated that a selective OSDA must exhibit both strong binding affinity toward the desired host and weak toward all other frameworks (*16*, *17*). To retroactively validate this hypothesis, we obtained 549 OSDAs from the literature using automated extraction tools (*18*, *19*). Then, we calculated the binding affinity of each OSDA toward 209 zeolite frameworks (Fig. S1 in the Supplementary Materials (SM)), thus generating a binding matrix (Methods, Figs. 1A, B). More than 586,000 zeolite-OSDA poses across different frameworks, OSDAs, loadings, and initial conformations were generated following the computational pipeline shown in Fig. 1C (*20*, *21*). By selecting the pose that optimized the binding energy for each OSDA-zeolite pair, we obtained a binding matrix with ~112,400 entries. Phase selectivity was then quantified by comparing OSDAs and zeolites across the rows and columns of the binding matrix using two metrics: the *directivity* of an OSDA (*D*), or how close a molecule is to the best OSDA for a given framework, and the *competitivity* of a framework (*C*), or how close a zeolite is to the best host for the given OSDA (Methods, Fig. 1B). These quantities did not necessarily correlate with the conventional binding energies (Fig. S2). As both the directivity and competitivity metrics were useful for optimizing zeolite-OSDA pairs, it was convenient to unify them under a single one-dimensional descriptor. We defined a quantity called templating energy (E_T) from the geometric mean of the Boltzmann average of each energy metric,

$$\mathrm{E_T} = -\mathrm{kT}\ \log(C_{\mathrm{OSDA}} D_{\mathrm{OSDA}} C_{\mathrm{SiO2}} D_{\mathrm{SiO2}})^{1/4},$$

where T is a temperature, k is the Boltzmann constant, and C (D) is the metric of competition (directivity) normalized either by OSDA or SiO_2 (Methods). The templating energy quantifies the notion that a particular zeolite-OSDA pair is better over another if both the competition and directivity energies are favorable according to both normalizations (Fig. S3).

The simulation data was then benchmarked on its ability to reproduce the 1,122 zeolite-OSDA pairs extracted from the literature. We used the templating energy to rank the best OSDAs for a given zeolite, and the best zeolites for a given OSDA. Because pairs not observed in the literature did not represent true negative data, only positive data points were used to assess the ranking scheme. Literature recall was quantified by plotting the cumulative number of positive OSDA-zeolite pairs recalled against the molecule/zeolite percentile (Fig. S4). A perfect agreement

between the binding metric and the literature data would lead to an area under the recall curve (AUC) equal to 1, and a random metric would have an AUC of 0.5. Fig. 1D exemplifies the recall curve for some zeolites and OSDAs. For zeolites such as **AEI** or ZSM-5 (**MFI**), the AUC values were high, suggesting that the positive pairs were systematically ranked high based on the templating energy metric. In fact, 34 of the 40 most common zeolite frameworks in the literature display AUC values higher than 0.5 (Fig. 1E), demonstrating that the ranking scheme reproduced past synthesis outcomes. Only OSDAs for a few frameworks, such as ZSM-12 (**MTW**) and mordenite (**MOR**), were not accurately recalled by the ranking scheme. These hosts are often synthesized through OSDA-free routes or with small amines, and thus are expected to appear as products in the presence of unselective OSDAs, with their synthesis dominated by factors beyond host-guest interactions, such as gel composition or temperature. Analogously to zeolites, the recall curves of OSDAs demonstrated that certain molecules were more selective than others. Smaller OSDAs typically have lower selectivity towards large cages and pores, and more complex, highly decorated OSDAs tend to be more selective (*22*). In keeping, zeotype structures have recall AUC on average 10% lower than their zeolite counterparts (Fig. 1E), as AlPO-type structures are frequently synthesized from smaller, less selective OSDAs (*22*). Additionally, a lower agreement between the literature and the binding metrics for certain frameworks suggested that binding energy metrics alone were limited predictors of synthesis outcomes in the context of Al-rich zeolites or dual OSDA design. This is the case of zeolite A (**LTA**), for instance, which is typically synthesized using tetramethylammonium to selectively direct the formation of sod cages in combination with another OSDA to direct the formation of the lta cage (*23*), or CIT-1 (**CON**), whose intersecting pores allow OSDAs to create molecular aggregates that direct crystallization (*24*).

Finally, we demonstrated that the templating energy metric outperformed plain binding energies in recalling positive data points from the literature (Fig. 1F). When selecting molecules for a given zeolite, the templating energy explained the literature better for ca. 70% of the structures, for which the average improvement in AUC was 0.06 with respect to the binding energy per framework atom, which is the traditional metric of OSDA-zeolite affinity (Fig. S5). On the other hand, the best hosts for a given OSDA were not well predicted by the templating energy, as the directivity component did not influence the structure-directing ability of an OSDA. Thus, we

propose both a single aggregate parameter to design OSDAs that is effective for screening, and independent energy metrics from which further insights could be derived.

OSDA design through phase competition and shape analysis

OSDAs must satisfy other design targets beyond binding energies. Physical descriptors of the OSDA molecular structure, for instance, are useful predictors of templating ability and complement phase competition metrics (*25*). Often, the strongest host-guest interactions occur for well-defined OSDA volumes or shapes, but their interplay is not necessarily bijective. To describe the shape of OSDAs with low-dimensional parameters, we performed a principal component analysis (PCA) of the three-dimensional distribution of atomic coordinates of ground-state conformers into a two-dimensional space (see Methods, Fig. 2A). In addition, we calculated the volume of each OSDA by using a voxel-based approach on the same conformers (see Methods). The two PCA axes and the volume are useful parameters to describe the overall shape and size of a molecule, and can be used as filters when proposing new OSDAs.

Designing molecules with targeted shapes, sizes, and selectivity can be performed in a purely computational manner, but other performance metrics of OSDAs, such as synthetic accessibility, are hard to evaluate algorithmically. In contrast, desiderata such as intellectual novelty of molecules are more easily recognized by experts, whereas quantitative templating metrics are not. A human-computer partnership drastically accelerates the process of molecular design by combining chemical intuition with computationally selected leads (*26*, *27*). To navigate and visualize hundreds of thousands of zeolite-OSDA pairs and leverage shape similarity, chemical intuition, and domain expertise, we created an online database of zeolite-OSDA pairs containing all simulation outcomes of this work. This database, called Organic Structure-directing agent DataBase (OSDB), provides a graphical interface to query, select, and compare molecules, as well as obtain information about prior art in the extracted literature and patents (Fig. S6 and Movie S1). Thus, all relevant design metrics were easily filtered and visualized in OSDB, allowing a computer-augmented design of OSDAs for targeted zeolites using interactive downselection of candidates (Movie S1). We illustrate this design process with several examples.

Based on the AUC analysis, our proposed metric showed high explanatory power for the small-pore zeolite **AEI**. The synthesis of the aluminosilicate SSZ-39 with **AEI** framework is typically carried out using alkyl-substituted piperidinium cations as OSDAs, such as the computationally

designed N-ethyl-N-methyl-2,2,6,6-tetramethylpiperidinium (OSDA **1**) (*28*), or the commercial N,N-diethyl-2,6-dimethylpiperidinium (OSDA **2**) (*29*) (Fig. 2B). According to our simulations, both OSDAs had favorable shapes for the **AEI** zeolite, with the nearly 1:1 aspect ratio at which binding affinities towards this framework were stronger (Fig. 2C). In fact, most OSDAs that are able to synthesize **AEI** with zeolite composition appeared at the top left region of the shape space, suggesting that shape and templating ability were indeed correlated for this zeolite (Fig. 2C). Furthermore, OSDAs **1** and **2** exhibit excellent templating energy and volume to fill the aei cage (200-225 $Å^3$) (Fig. 2D). Nevertheless, their synthetic complexity, quantified by the SCScore proposed by Coley *et al.* in (*30*), was higher than that of many other known or candidate OSDAs (Fig. 2E), suggesting higher preparation costs. In particular, the lower SCScore of OSDA **2** compared to OSDA **1** could be related to its usage as commercial template for the industrial preparation of SSZ-39.

Based on the design strategies summarized by Fig. 2 and visualized in OSDB (Movie S1), we proposed tris(dimethylamino)(methyl)phosphonium (OSDA **3**) as a new candidate for the synthesis of SSZ-39. It not only displayed favorable volume (Fig. 2D) and phase competition metrics (Fig. S7) toward the **AEI** framework, but also showed considerably lower synthetic complexity than piperidinium-type cations (Fig. 2E). Following this lead, SSZ-39 was first prepared using OSDA **3** under the following synthesis conditions: 1 SiO_2 : 0.036 Al_2O_3 : 0.3 OSDA **3** : 0.2 NaOH : 15 H_2O, using the high-silica **FAU** CBV720 as the Si/Al source, and with the crystallization carried out at 135 °C for 7 days. The main physicochemical characteristics of this material are summarized in Fig. S8, showcasing tetrahedrally-coordinated Al species in framework positions, as well as crystalline nature and textural properties comparable with an **AEI** zeolite synthesized with baseline commercial OSDAs.

We evaluated the selectivity of computationally designed OSDA **3** by comparing its ability to crystallize **AEI** against a known, also phosphorous-containing template for this framework, tetraethylphosphonium (OSDA **4**). Instead of using the high-silica **FAU** zeolite (Zeolyst, CBV720) as the Si and Al source, we used fumed silica as Si source and the low-silica **FAU** (CBV500) as the Al source, thus lowering the overall cost of the synthesis, but increasing the difficulty in crystallizing the target zeolite. The synthesis of SSZ-39 was attempted under the following conditions: 1 SiO_2 : 0.091 or 0.125 Al_2O_3 : 0.2 OSDA **3** or **4** : 0.25 NaOH : 5 H_2O. Although OSDA **4** did not yield **AEI** in either of these conditions, OSDA **3** successfully crystallized SSZ-

39 in both (Fig. S9), attesting to the higher selectivity of the latter towards **AEI**. Although both OSDAs display similar shapes, OSDA **3** is closer to the ideal OSDA **1** than OSDA **4** (Fig. 2B), exhibiting more favorable templating and competition energies by about 1 kJ/mol and 5 kJ/mol SiO_2, respectively. These values suggested that the proposed computational metrics were effective in capturing the subtleties of template selectivity during the OSDA design process despite the fine resolution of the zeolite-OSDA interaction energies. Our binding metrics were also effective at singling out highly selective OSDAs that led to the discovery of frameworks such as **MFI**, ITQ-4 (**IFR**), and ITQ-7 (**ISV**) (Fig. S10). These results suggested that the proposed tools could not only identify new OSDAs for known structures, but hold potential to detect archetypical templates for unrealized zeolite topologies.

As a second example, we analyzed the interplay between OSDA shape and binding metrics in the experimental phase selectivity of **CHA**. Aluminosilicate **CHA** (SSZ-13) is typically synthesized using N,N,N-trimethyladamantammonium (TMAda, denoted here as OSDA **5**), a relatively expensive and complex OSDA (*31*) (Fig. 3A). Beyond TMAda, N-ethyl-N,N-dimethylcyclohexanaminium (OSDA **7**) has also been described for the synthesis of SSZ-13 as a simpler OSDA (*32, 33*). Accordingly, our descriptors indicated that OSDAs **5** and **7** displayed similar shapes (Fig. 3B) and synthesis complexity (Fig. 3D), although OSDA **5** was closer to the ideal volume of 210 $Å^3$ than OSDA **7** (Figs. 3C).

To probe the influence of shape in the phase selectivity of zeolites, we compared the ability of OSDA **7** to synthesize **CHA** with that of N,N,N-trimethylcyclohexanaminium (OSDA **6**) (*34*) and N,N-diethyl-N-methylcyclohexanaminium (OSDA **8**) (*35*). OSDAs **6**-**8** had favorable binding and templating energies towards **CHA** (Fig. S11) and were effective templates for this framework. Although they are chemically similar, their geometrical shapes were significantly different within the precision of our descriptors (Fig. 3B), and their binding strengths increased from OSDA **6** through **8**. A design approach considering only the binding metrics would predict OSDA **8** as the best template for **CHA**. To verify this hypothesis, we attempted the synthesis of SSZ-13 using these three templates under a variety of conditions, including using amorphous or high-silica crystalline Si and Al sources, different Si/Al and Na/Si ratios, and with/without the presence of seeds (Fig. S12). As expected by its less favorable templating energy and poorer geometrical fit, OSDA **6** showed the narrowest synthesis windows among the three templates, being unable to fully crystallize **CHA** when high-silica **FAU** was used as a Si source under Na-free conditions

(Fig. S12A), or in most syntheses using amorphous sources (Figs. S12B,C). Remarkably, OSDA **7** outperformed OSDA **8** in more demanding synthesis conditions (Fig. S12D), despite OSDA **7** having the weaker binding energy of the two. These results indicated that other effects may lower the experimental selectivity of OSDA **8** towards **CHA** compared to OSDA **7**. For example, the shape of OSDA **8** is further away from the ideal shape of OSDA **5** than OSDA **7**. When OSDA **8** was occluded in the **CHA** cage, its shape experienced larger geometrical distortions to achieve the final, occluded conformation (Fig. S13), which increased its free energy and reduced its ability to crystallize **CHA**. Thus, designing OSDAs with appropriate shapes and volumes may be as important as optimizing binding energies for improving phase selectivity in zeolite synthesis, particularly when molecules already exhibit favorable competition metrics towards the targeted frameworks.

Modulating aluminum distributions through OSDA design

Although dispersion interactions typically provide framework selectivity (*22*), electrostatic interactions between the framework and structure-directing agents rule heteroatom distributions, influencing the stability and catalytic properties of the product zeolite (*36–38*). OSDAs with strong affinity and distinct charge distribution may overcome natural aluminum biases and crystallize desired frameworks with tailored aluminum distributions. To screen for charge distribution in OSDAs without using electronic structure calculations, we proposed a geometric descriptor by taking the distance between the quaternary nitrogen atom in a monocationic OSDA to the center of the mass of the molecule (Fig. S14A). This descriptor allowed us to compare molecules with different charge distributions and templating abilities toward **CHA** (Fig. S14C). Accordingly, the commercially available tetraethylammonium (OSDA **9**) and spiro-type molecules (OSDAs **10**-**13**) were molecules with good templating energy for the synthesis of SSZ-13, and have charge distributions that significantly differ from TMAda (Figs. 3A, S14C). Although alkyl-substituted spiro-type OSDAs have been used for the synthesis of **CHA** before (*39*), alkyl groups increase the complexity of the organic synthesis, potentially adding purification/separation steps, decreasing the overall product yields, and increasing the costs. Furthermore, alkyl substituents result in uncontrolled diastereomeric mixtures, which can have a dramatic influence on the zeolite nucleation/crystallization processes (*40, 41*). On the other hand, non-substituted spiro-type molecules are more easily prepared, as reflected by their lower SCScores compared to that of

OSDA **5** (Figs. 3D). In particular, the 6-azaspiro[5.6]dodecan-6-ium (OSDA **12**) had a near-ideal volume for **CHA** (Fig. 3C). Although its templating energy was higher than that of OSDA **5**, it was comparable with the commercial OSDA **7**, and lay near the Pareto frontier between templating energy and SCScore for OSDAs in **CHA** (Fig. 3D). This fact implied OSDA **12** offered one of the best trade-offs between templating ability and synthetic complexity among the candidates studied in this work, in addition to its distinctive charge distribution. Furthermore, despite been previously described as an OSDA unable to synthesize **CHA** in various conditions (*42*), our calculations showed that OSDA **12** had favorable competition metrics toward **CHA** (Fig. S15).

Based on these predictions, the synthesis of **CHA** using OSDA **12** was first performed using the following synthesis gel composition: 1 SiO_2 : 0.036 Al_2O_3 : 0.2 OSDA **12** : 0.3 NaOH : 15 H_2O at 150 °C for 12 days, where the high-silica **FAU** CBV720 was used as the Si/Al source. The main physico-chemical characteristics of this material are summarized in Fig. S16, where the tetrahedrally-coordinated Al species in framework positions are demonstrated along with crystalline nature and textural properties similar to the baseline **CHA** (std). With this successful proof-of-concept, we compared the effect of templating for the broader family of spiro-type OSDAs **10**-**13** using our binding metrics and a wider range of synthesis conditions. Figure S17A shows that OSDAs **10** and **13** were unable to crystallize **CHA** in the synthesis conditions tested, as predicted by their unfavorable shapes, volumes, templating energies, and phase selectivity towards **CHA** (Figs. 3B,C and Fig. S15). On the other hand, OSDAs **11** and **12** displayed more favorable phase selectivity towards **CHA** and successfully crystallized the framework (Fig. S17A). In particular, a better pore-filling effect from OSDA **12**, as evidenced by its larger volume, improved its selectivity towards SSZ-13 and exhibited a larger synthesis window, despite the comparable templating energies between OSDA **11** and **12**. In addition, OSDA **12** was able to crystallize **CHA** in more demanding conditions, such as using amorphous or Al-rich crystalline sources (Figs. S17D,E).

We then performed density functional theory (DFT) calculations, which explicitly accounts for electrostatics (*21*), to analyze the distribution of aluminum sites in the cha cage as a function of the OSDA (see Methods). Because sodium is typically present in the reaction medium, it was included explicitly in the simulations as a co-template. By computing the relative energies of 48 different Al pairs for each molecule (*43*) (Fig. S18), we found that different OSDAs imprinted different aluminum distribution onto the material (Figs. 3E, S19). Assuming that the Al sites

distributed themselves in the framework at the thermodynamic equilibrium of OSDA-zeolite interactions, energy differences could be translated into ensemble probabilities for the Al distribution at a given temperature (433 K in Figs. 3E, S19). Although kinetic factors beyond OSDAs can also bias aluminum distributions, this equilibrium assumption stroke balance between accuracy and computational cost and enabled comparing how OSDAs influenced aluminum pairing quantitatively and predictively. For the particular case of **CHA**, the equilibrium distribution of aluminum sites was found to be highly sensitive to the OSDA spatial charge distribution, and the nitrogen center descriptor showed a linear relationship with the fraction of aluminum pairs expected in d6r units (Fig. 3F). OSDAs with the nitrogen center closer to the center of the cha cage, such as OSDAs **9** or **12**, were less likely to form paired sites in the d6r units compared to the more polarized OSDAs **5**-**7**. Interestingly, OSDA **8** directed the formation of fewer paired aluminum sites in the d6r than OSDA **7** due to a larger distance between the nitrogen and the d6r unit imposed by the two ethyl groups. While disentangling the effects of electrostatic and shape in the **CHA** (OSDA **8**) synthesis is not straightforward, the nearly equivalent charge distributions of OSDAs **5**, **6**, and **7** support the fact that the differences in phase selectivity between the three OSDAs were due to templating effects rather than electrostatics.

Co-templating of OSDA **12** and Na^+ was predicted to yield significantly fewer aluminum pairs in d6r units compared to cha cages synthesized with OSDA **5** and Na^+. To verify these predictions, we performed cobalt titration experiments to quantify Al pairing in **CHA** samples with similar physico-chemical characteristics but synthesized with different OSDAs (Methods). Although cobalt titrations cannot fully characterize aluminum pairs due to uncertainties intrinsic to the technique, they are often useful for uncovering trends between samples (*44*). **CHA** crystals synthesized with OSDA **5** showed, on average, 3.4 ± 0.8 times more Co^{2+} ions per aluminum than counterparts synthesized by OSDA **12** (Fig. 3F, inset, see also Fig. S20). This result was in quantitative agreement with the 3.05 ratio predicted by DFT and demonstrates that the newly proposed OSDA **12** provided a different aluminum bias when synthesizing **CHA**. As paired aluminum sites in the 8-membered ring of the cha cage are more relevant for catalytic applications (*38*), OSDA **12** may enhance the catalytic properties of **CHA** zeolites. Hence, controlling the distribution of aluminum sites through OSDA design may be a pathway to improve the performance of zeolite catalysts.

Finally, to analyze the co-templating effect of sodium as the inorganic structure-directing agent, we used OSDA **12** with potassium hydroxide in the synthesis media. In these experiments, **CHA** was absent, and the **EAB** framework was detected instead (Fig. S17E). Interestingly, OSDA **12** had the same binding energy towards the main cavities of both zeolites (-183 kJ/mol OSDA). We surmise that since the K^+ ion is too large to occupy the d6r position as directed by Na^+ (*43*), the gme cage of **EAB** zeolite is favored instead. Therefore, the final zeolite crystallized by OSDA **12** had cages that solvated the template equally well, but the cooperation between inorganic and organic SDAs determined the other building units that crystallized the framework around the OSDA. This fact suggests that quantifying phase competition beyond zeolite-OSDA interactions could move the field beyond expert-informed selection of inorganic conditions and towards a fully automated prediction of zeolite synthesis.

OSDA design for intergrown zeolites

Intergrown zeolites offer distinctive properties compared to pure zeolite phases, such as different diffusional pathways and molecule confinements, or particular crystallographic environments to incorporate metallic active sites (*45*–*47*). Among the intergrown catalysts of industrial relevance, the silicoaluminophosphate (SAPO) form of **CHA**/**AEI** has shown distinct product selectivity and catalyst lifetime for the methanol-to-olefins (MTO) process compared to the pure crystalline **CHA** and **AEI** phases (*48*, *49*). Yet, SAPO-type catalysts have smaller hydrolytic and hydrothermal stability, as well as lower acidity compared to aluminosilicate zeolites. High-silica, intergrown small-pore zeolites (e.g. **AFX**/**CHA**) are often prepared using mixtures of OSDAs favorable for each individual zeolite (*50*, *51*). However, this dual OSDA approach requires empirically fine-tuning the synthesis parameters to avoid the crystallization of two independent zeolite phases, drastically increasing the complexity and cost of the process. To obtain a low-cost, aluminosilicate **CHA**/**AEI** intergrowth, we used our tools to design a single OSDA that crystallizes the targeted intergrown structure.

Based on the interplay between shape and binding shown in this work, we hypothesized that designing an OSDA for a targeted intergrowth required not only balancing phase competition, but also controlling the synthesis of structural motifs in the frameworks of interest (*52*). Figure 4A compares the binding energies of OSDAs toward **AEI**, **CHA**, and all other zeolites. Most of the OSDAs that synthesized **AEI** were indeed more favorable toward this framework than toward

CHA, as expected from our AUC analysis and traditional phase competition assumptions (*17*). The selectivity of OSDAs **1**, **3**, **5**, and **12** to their product phases was also demonstrated by their distance from the equal-energy diagonal and low competition energy. Remarkably, the simulation outcomes revealed a phase boundary in the OSDA shape landscape (Fig. 4B). Stronger binders towards **AEI** fell within the region of OSDAs with aspect ratio closer to 1:1, and longer molecules favored the **CHA** framework. Differences of binding energies of OSDAs toward **CHA** and **AEI** highlighted these two distinct domains, shown in Fig. 4B with red and blue colors, respectively. From these two principles and after data exploration in OSDB (Movie S1), we selected N-ethyl-N-isopropyl-N-methylpropan-2-aminum (OSDA **14**) as a potential candidate to direct the crystallization of the **CHA**/**AEI** intergrowth. OSDA **14** had comparable binding energies to both pure phases (Fig. S21), and its shape lay on the phase boundary between the two frameworks. In fact, OSDA **14** resembled an interpolation between the best OSDAs for **AEI** (OSDA **1**) and **CHA** (OSDA **5**) both in the shape space (Fig. 4B) and when the OSDAs are visualized with their charge densities (Fig. 4C).

Based on this theoretical lead, a **CHA**/**AEI** intergrowth was prepared under synthesis conditions similar to the ones successfully used in the previous examples: 1 SiO_2 : 0.036 Al_2O_3 : 0.3 OSDA **14** : 0.2 NaOH : 15 H_2O, with the crystallization carried out at 140 °C for 5 days. The PXRD pattern of the as-prepared material showed broadened peaks at angles mainly characteristic of **CHA** (Fig. 4D). Additional smeared peaks also appeared at angles compatible with the **AEI** phase, confirming the presence of both phases in the solid. To rule out the presence of a physical mixture of crystalline particles, the as-prepared sample was imaged by scanning electron microscopy, revealing uniform particles with average size of ~200 nm (Fig. S22A). OSDA **14** molecules remained intact after the hydrothermal synthesis of the **CHA/AEI** (OSDA **14**) sample (Table S1, Fig. S22B). The PXRD pattern of the calcined form of **CHA**/**AEI** (OSDA **14**) indicated that the sample was formed by a 50:50 **CHA**:**AEI** intergrowth as compared to DIFFaX simulations (Figs. S23 and S24). High-resolution scanning transmission electron microscopy images confirmed the intergrowth structure (Fig. 4E), showing an alternating stacking sequence caused by the orientation of the d6r units in **CHA** and **AEI** frameworks. The intergrowth **CHA**/**AEI** material showed a Si/Al molar ratio of 11 (Table S2), and micropore volume of ~0.28 cm^3/g, similar to the pure **AEI** and **CHA** materials.

To illustrate the application of the intergrowth, the structure was tested as a catalyst for the MTO reaction at 350 °C (Fig. 4F). The X_{95} catalyst lifetime observed for the **CHA**/**AEI** (OSDA **14**) material was 788 min, which was similar to that of the **CHA** (OSDA **12**) catalyst reported in this work. We speculate that different active site distributions along cha and aei cavities influenced the overall diffusion pathways of the reaction-involved light olefins, thus affecting the catalyst deactivation mechanisms. However, more fundamental characterization work should be done to elucidate this phenomenon. Regarding product selectivity, the **CHA**/**AEI** intergrowth showed the production of equivalent amounts of ethylene and propylene (~40-42%, see Table S3 and Fig. S25) and ~16% of butene (see Table S3). These olefin selectivities were in-between the values achieved for the pure phases (Fig. 4G), as also shown by the $C_3^=/C_2^=$ and $C_4^=/C_2^=$ ratios (Table S3), further supporting the claim that the product selectivity for the MTO reaction was governed by the zeolite cages present in the final intergrown crystals.

Conclusions

High-throughput computation allows controlling phase competition in zeolite synthesis beyond Edisonian approaches that have dominated zeolite synthesis to date. Proposed metrics of phase competition, retroactively validated on comprehensive literature data, identified selective OSDAs through energetic, geometric, and electrostatic arguments. In three examples, competition was suppressed by designing OSDAs with favorable shapes, sizes, and binding metrics, achieving pure phases with wider synthesis windows. Reciprocally, it was possible to tailor intergrowths by designing a single OSDA that balanced phase competition both through shape and binding metrics. The ability of the method to recover literature outcomes from non-charged simulations suggested that product zeolites could often be predicted using only dispersion interactions. However, the final product is often dependent on co-templating effects between inorganic and organic SDAs. In addition, tuning OSDA charge and polarization modulates the aluminum distribution of the crystallized **CHA** zeolite, which can have important implications for catalysis. The computational results on templating effects can be further used to train data-driven selectivity models based on molecular structure descriptors, increasing the breadth of high-throughput screening undertakings. At the same time, developing more general electrostatic descriptors may also guide the investigation of aluminum distributions in zeolites beyond **CHA**. Finally, interactive visualization

and analysis of said data through the OSDB portal is expected to empower domain experts to leverage these advances and accelerate the discovery cycle of zeolites.

References and Notes:

1. W. Vermeiren, J.-P. Gilson, Impact of Zeolites on the Petroleum and Petrochemical Industry. *Top. Catal.* **52**, 1131–1161 (2009).
2. Y. Li, L. Li, J. Yu, Applications of Zeolites in Sustainable Chemistry. *Chem*. **3**, 928–949 (2017).
3. M. Moliner, F. Rey, A. Corma, Towards the Rational Design of Efficient Organic Structure-Directing Agents for Zeolite Synthesis. *Angew. Chemie Int. Ed.* **52**, 13880–13889 (2013).
4. P. Eliášová, M. Opanasenko, P. S. Wheatley, M. Shamzhy, M. Mazur, P. Nachtigall, W. J. Roth, R. E. Morris, J. Čejka, The ADOR mechanism for the synthesis of new zeolites. *Chem. Soc. Rev.* **44**, 7177–7206 (2015).
5. E. M. Gallego, M. T. Portilla, C. Paris, A. León-Escamilla, M. Boronat, M. Moliner, A. Corma, "Ab initio" synthesis of zeolites for preestablished catalytic reactions. *Science.* **355**, 1051–1054 (2017).
6. D. W. Lewis, D. J. Willock, C. R. A. Catlow, J. M. Thomas, G. J. Hutchings, De novo design of structure-directing agents for the synthesis of microporous solids. *Nature*. **382**, 604–606 (1996).
7. G. Sastre, A. Cantin, M. J. Diaz-Cabañas, A. Corma, Searching Organic Structure Directing Agents for the Synthesis of Specific Zeolitic Structures: An Experimentally Tested Computational Study. *Chem. Mater.* **17**, 545–552 (2005).
8. J. E. Schmidt, M. W. Deem, M. E. Davis, Synthesis of a Specified, Silica Molecular Sieve by Using Computationally Predicted Organic Structure-Directing Agents. *Angew. Chemie Int. Ed.* **53**, 8372–8374 (2014).
9. F. Daeyaert, F. Ye, M. W. Deem, Machine-learning approach to the design of OSDAs for zeolite beta. *Proc. Natl. Acad. Sci. U. S. A.* **116**, 3413–3418 (2019).
10. K. Muraoka, W. Chaikittisilp, T. Okubo, Multi-objective de novo molecular design of organic structure-directing agents for zeolites using nature-inspired ant colony optimization. *Chem. Sci.* **11**, 8214–8223 (2020).

11. R. Pophale, F. Daeyaert, M. W. Deem, Computational prediction of chemically synthesizable organic structure directing agents for zeolites. *J. Mater. Chem. A.* **1**, 6750–6760 (2013).

12. K. Muraoka, Y. Sada, D. Miyazaki, W. Chaikittisilp, T. Okubo, Linking synthesis and structure descriptors from a large collection of synthetic records of zeolite materials. *Nat. Commun.* **10**, 4459 (2019).

13. Ch. Baerlocher and L.B. McCusker, Database of Zeolite Structures, http://www.iza-structure.org/databases/ (2021).

14. M. M. J. Treacy, I. Rivin, E. Balkovsky, K. H. Randall, M. D. Foster, Enumeration of periodic tetrahedral frameworks. II. Polynodal graphs. *Microporous Mesoporous Mater.* **74**, 121–132 (2004).

15. M. W. Deem, R. Pophale, P. A. Cheeseman, D. J. Earl, Computational Discovery of New Zeolite-Like Materials. *J. Phys. Chem. C*. **113**, 21353–21360 (2009).

16. P. Wagner, Y. Nakagawa, G. S. Lee, M. E. Davis, S. Elomari, R. C. Medrud, S. I. Zones, Guest/Host Relationships in the Synthesis of the Novel Cage-Based Zeolites SSZ-35, SSZ-36, and SSZ-39. *J. Am. Chem. Soc.* **122**, 263–273 (2000).

17. A. W. Burton, G. S. Lee, S. I. Zones, Phase selectivity in the syntheses of cage-based zeolite structures: An investigation of thermodynamic interactions between zeolite hosts and structure directing agents by molecular modeling. *Microporous Mesoporous Mater.* **90**, 129–144 (2006).

18. Z. Jensen, E. Kim, S. Kwon, T. Z. H. Gani, Y. Román-Leshkov, M. Moliner, A. Corma, E. Olivetti, A Machine Learning Approach to Zeolite Synthesis Enabled by Automatic Literature Data Extraction. *ACS Cent. Sci.* **5**, 892–899 (2019).

19. Z. Jensen, S. Kwon, D. Schwalbe-Koda, C. Paris, R. Gómez-Bombarelli, Y. Román-Leshkov, A. Corma, M. Moliner, E. A. Olivetti, Discovering Relationships between OSDAs and Zeolites through Data Mining and Generative Neural Networks. *ACS Cent. Sci.* **7**, 858–867 (2021).

20. D. Schwalbe-Koda, R. Gomez-Bombarelli, Supramolecular Recognition in Crystalline Nanocavities Through Monte Carlo and Voronoi Network Algorithms. *J. Phys. Chem. C.* **125**, 3009–3017 (2021).

21. D. Schwalbe-Koda, R. Gomez-Bombarelli, Benchmarking binding energy calculations for organic structure-directing agents in pure-silica zeolites. *J. Chem. Phys.* **154**, 174109 (2021).

22. R. F. Lobo, S. I. Zones, M. E. Davis, Structure-direction in zeolite synthesis. *J. Incl. Phenom. Mol. Recognit. Chem.* **21**, 47–78 (1995).

23. A. Corma, F. Rey, J. Rius, M. J. Sabater, S. Valencia, Supramolecular self-assembled molecules as organic directing agent for synthesis of zeolites. *Nature*. **431**, 287–290 (2004).

24. B. H. Toby, N. Khosrovani, C. B. Dartt, M. E. Davis, J. B. Parise, Structure-directing agents and stacking faults in the CON system: a combined crystallographic and computer simulation study. *Microporous Mesoporous Mater.* **39**, 77–89 (2000).

25. R. E. Boyett, A. P. Stevens, M. G. Ford, P. A. Cox, A quantitative shape analysis of organic templates employed in zeolite synthesis. *Zeolites*. **17**, 508–512 (1996).

26. R. Gómez-Bombarelli, J. Aguilera-Iparraguirre, T. D. Hirzel, D. K. Duvenaud, D. Maclaurin, M. A. Blood-Forsythe, H. S. Chae, M. Einzinger, D.-G. G. Ha, T. Wu, G. Markopoulos, S. Jeon, H. Kang, H. Miyazaki, M. Numata, S. Kim, W. Huang, S. I. Hong, M. Baldo, R. P. Adams, A. Aspuru-Guzik, Design of efficient molecular organic light-emitting diodes by a high-throughput virtual screening and experimental approach. *Nat. Mater.* **15**, 1120–1127 (2016).

27. M. Moliner, Y. Román-Leshkov, A. Corma, Machine Learning Applied to Zeolite Synthesis: The Missing Link for Realizing High-Throughput Discovery. *Acc. Chem. Res.* **52**, 2971–2980 (2019).

28. J. E. Schmidt, M. W. Deem, C. Lew, T. M. Davis, Computationally-Guided Synthesis of the 8-Ring Zeolite AEI. *Top. Catal.* **58**, 410–415 (2015).

29. S. I. Zones, Y. Nakagawa, S. T. Evans, G. S. Lee, Zeolite SSZ-39. *US Pat. 5,958,370* (1999).

30. C. W. Coley, L. Rogers, W. H. Green, K. F. Jensen, SCScore: Synthetic Complexity Learned from a Reaction Corpus. *J. Chem. Inf. Model.* **58**, 252–261 (2018).

31. S. I. Zones, Conversion of faujasites to high-silica chabazite SSZ-13 in the presence of N,N,N-trimethyl-1-adamantammonium iodide. *J. Chem. Soc. Faraday Trans.* **87**, 3709–3716 (1991).

32. G. Cao, M. M. Mertens, A. S. Guram, H. Li, J. C. Yoder, Synthesis of chabazite-containing

molecular sieves and their use in the conversion of oxygenates to olefins. *US Pat. 7,754,187* (2007).

33. X. Wang, Q. Wu, C. Chen, S. Pan, W. Zhang, X. Meng, S. Maurer, M. Feyen, U. Müller, F.-S. Xiao, Atom-economical synthesis of a high silica CHA zeolite using a solvent-free route. *Chem. Commun.* **51**, 16920–16923 (2015).

34. T. M. Davis, S. Elomari, S. I. Zones, Method for preparing cha-type molecular sieves using colloidal aluminosilicate. *US Pat. 2014/0147378* (2014).

35. G. Cao, M. Mertens, A. S. Guram, H. Li, J. C. Yoder, Synthesis of chabazite-containing molecular sieves and their use in the conversion of oxygenates to olefins. *US Pat. 2008/0045767* (2008).

36. J. R. Di Iorio, C. T. Nimlos, R. Gounder, Introducing Catalytic Diversity into Single-Site Chabazite Zeolites of Fixed Composition via Synthetic Control of Active Site Proximity. *ACS Catal.* **7**, 6663–6674 (2017).

37. E. M. Gallego, C. Li, C. Paris, N. Martín, J. Martínez-Triguero, M. Boronat, M. Moliner, A. Corma, Making Nanosized CHA Zeolites with Controlled Al Distribution for Optimizing Methanol-to-Olefin Performance. *Chem. – A Eur. J.* **24**, 14631–14635 (2018).

38. F. Göltl, S. Bhandari, M. Mavrikakis, Thermodynamics Perspective on the Stepwise Conversion of Methane to Methanol over Cu-Exchanged SSZ-13. *ACS Catal.*, 7719–7734 (2021).

39. Y. Nakagawa, G. S. Lee, T. V. Harris, L. T. Yuen, S. I. Zones, Guest/host relationships in zeolite synthesis: Ring-substituted piperidines and the remarkable adamantane mimicry by 1-azonio spiro [5.5] undecanes. *Microporous Mesoporous Mater.* **22**, 69–85 (1998).

40. M. Dusselier, J. E. Schmidt, R. Moulton, B. Haymore, M. Hellums, M. E. Davis, Influence of Organic Structure Directing Agent Isomer Distribution on the Synthesis of SSZ-39. *Chem. Mater.* **27**, 2695–2702 (2015).

41. C. Kim, S.-J. Hwang, A. W. Burton, S. I. Zones, A case study of divergent structure directing effects of geometric isomers: The discovery of a new structure directing agent for an all-silica RTH zeolite prepared in fluoride media. *Microporous Mesoporous Mater.* **116**, 227–232 (2008).

42. R. Millini, L. Carluccio, F. Frigerio, W. O'Neil Parker, G. Bellussi, Zeolite synthesis in the

presence of azonia-spiro compounds as structure-directing agents. *Microporous Mesoporous Mater.* **24**, 199–211 (1998).

43. J. R. Di Iorio, S. Li, C. B. Jones, C. T. Nimlos, Y. Wang, E. Kunkes, V. Vattipalli, S. Prasad, A. Moini, W. F. Schneider, R. Gounder, Cooperative and Competitive Occlusion of Organic and Inorganic Structure-Directing Agents within Chabazite Zeolites Influences Their Aluminum Arrangement. *J. Am. Chem. Soc.* **142**, 4807–4819 (2020).

44. J. R. Di Iorio, R. Gounder, Controlling the Isolation and Pairing of Aluminum in Chabazite Zeolites Using Mixtures of Organic and Inorganic Structure-Directing Agents. *Chem. Mater.* **28**, 2236–2247 (2016).

45. H. Kosslick, H. Berndt, H. D. Lanh, A. Martin, H. Miessner, V. A. Tuan, J. Jänchen, Acid properties of ZSM-20-type zeolite. *J. Chem. Soc. Faraday Trans.* **90**, 2837–2844 (1994).

46. T. Willhammar, J. Sun, W. Wan, P. Oleynikov, D. Zhang, X. Zou, M. Moliner, J. Gonzalez, C. Martínez, F. Rey, A. Corma, Structure and catalytic properties of the most complex intergrown zeolite ITQ-39 determined by electron crystallography. *Nat. Chem.* **4**, 188–194 (2012).

47. J. S. Bates, B. C. Bukowski, J. W. Harris, J. Greeley, R. Gounder, Distinct Catalytic Reactivity of Sn Substituted in Framework Locations and at Defect Grain Boundaries in Sn-Zeolites. *ACS Catal.* **9**, 6146–6168 (2019).

48. L. Guo, W. Zhu, P. Miao, F. Li, Z. Guo, Q. Sun, Intergrowth Silicoaluminophosphate Molecular Sieves Synthesized and Their Catalytic Performances for Methanol to Olefins Reaction. *Ind. Eng. Chem. Res.* **57**, 10398–10402 (2018).

49. R. L. Smith, S. Svelle, P. del Campo, T. Fuglerud, B. Arstad, A. Lind, S. Chavan, M. P. Attfield, D. Akporiaye, M. W. Anderson, CHA/AEI intergrowth materials as catalysts for the Methanol-to-Olefins process. *Appl. Catal. A Gen.* **505**, 1–7 (2015).

50. Y. Naraki, K. Ariga, K. Nakamura, K. Okushita, T. Sano, ZTS-1 and ZTS-2: Novel intergrowth zeolites with AFX/CHA structure. *Microporous Mesoporous Mater.* **254**, 160–169 (2017).

51. G. Cao, M. M. Mertens, K. G. Strohmaier, R. B. Hall, T. H. Colle, M. Afeworki, A. J. Bons, W. J. Mortier, C. Kliewer, H. Li, A. S. Guram, R. J. Saxton, M. T. Muraoka, J. C. Yoder, Chabazite-containing molecular sieve, its synthesis and its use in the conversion of

oxygenates to olefins. *US Pat. 7,094,389 B2* (2006).

52. D. Schwalbe-Koda, Z. Jensen, E. Olivetti, R. Gómez-Bombarelli, Graph similarity drives zeolite diffusionless transformations and intergrowth. *Nat. Mater.* **18**, 1177–1181 (2019).

53. J. Towns, T. Cockerill, M. Dahan, I. Foster, K. Gaither, A. Grimshaw, V. Hazlewood, S. Lathrop, D. Lifka, G. D. Peterson, R. Roskies, J. Scott, N. Wilkins-Diehr, XSEDE: Accelerating Scientific Discovery. *Comput. Sci. Eng.* **16**, 62–74 (2014).

54. D. Schwalbe-Koda, learningmatter-mit/VOID: VOID 1.0.1. *Zenodo* (2021), doi:10.5281/zenodo.5260054.

55. D. Schwalbe-Koda, learningmatter-mit/gulpy: GULPy 1.0. *Zenodo* (2021), doi:10.5281/zenodo.5260056.

56. B. Blaiszik, K. Chard, J. Pruyne, R. Ananthakrishnan, S. Tuecke, I. Foster, The Materials Data Facility: Data Services to Advance Materials Science Research. *JOM*. **68**, 2045–2052 (2016).

57. B. Blaiszik, L. Ward, M. Schwarting, J. Gaff, R. Chard, D. Pike, K. Chard, I. Foster, A data ecosystem to support machine learning in materials science. *MRS Commun.* **9**, 1125–1133 (2019).

58. D. Schwalbe-Koda, R. Gómez-Bombarelli, Data for: Ab initio control of zeolite synthesis and intergrowth with high-throughput simulations. *Mater. Data Facil.* (2021), doi:10.18126/c5z9-zej7.

59. D. Schwalbe-Koda, learningmatter-mit/Zeolite-Phase-Competition: Article data for: Ab initio control of zeolite phase competition and intergrowth with high-throughput simulations (1.0). *Zenodo*, doi:10.5281/zenodo.5272354.

60. J. D. Gale, GULP: A computer program for the symmetry-adapted simulation of solids. *J. Chem. Soc. Trans.* **93**, 629–637 (1997).

61. J. D. Gale, A. L. Rohl, The General Utility Lattice Program (GULP). *Mol. Simul.* **29**, 291–341 (2003).

62. M. J. Sanders, M. Leslie, C. R. A. Catlow, Interatomic potentials for SiO2. *J. Chem. Soc. Chem. Commun.*, 1271–1273 (1984).

63. G. Landrum, RDKit: Open-source cheminformatics, www.rdkit.org (2006).

64. T. A. Halgren, Merck molecular force field. I. Basis, form, scope, parameterization, and

performance of MMFF94. *J. Comput. Chem.* **17**, 490–519 (1996).

65. P. Tosco, N. Stiefl, G. Landrum, Bringing the MMFF force field to the RDKit: implementation and validation. *J. Cheminform.* **6**, 37 (2014).

66. S. L. Mayo, B. D. Olafson, W. A. Goddard, DREIDING: A generic force field for molecular simulations. *J. Phys. Chem.* **94**, 8897–8909 (1990).

67. G. Kresse, J. Furthmüller, Efficiency of ab-initio total energy calculations for metals and semiconductors using a plane-wave basis set. *Comput. Mater. Sci.* **6**, 15–50 (1996).

68. G. Kresse, J. Furthmüller, Efficient iterative schemes for ab initio total-energy calculations using a plane-wave basis set. *Phys. Rev. B.* **54**, 11169–11186 (1996).

69. P. E. Blöchl, Projector augmented-wave method. *Phys. Rev. B.* **50**, 17953–17979 (1994).

70. G. Kresse, D. Joubert, From ultrasoft pseudopotentials to the projector augmented-wave method. *Phys. Rev. B.* **59**, 1758–1775 (1999).

71. J. P. Perdew, K. Burke, M. Ernzerhof, Generalized Gradient Approximation Made Simple. *Phys. Rev. Lett.* **77**, 3865–3868 (1996).

72. C. J. Heard, L. Grajciar, P. Nachtigall, The effect of water on the validity of Löwenstein's rule. *Chem. Sci.* **10**, 5705–5711 (2019).

73. M. M. J. Treacy, J. M. Newsam, M. W. Deem, A general recursion method for calculating diffracted intensities from crystals containing planar faults. *Proc. R. Soc. London. Ser. A Math. Phys. Sci.* **433**, 499–520 (1991).

74. P. Ferri, C. Li, R. Millán, J. Martínez-Triguero, M. Moliner, M. Boronat, A. Corma, Impact of Zeolite Framework Composition and Flexibility on Methanol-To-Olefins Selectivity: Confinement or Diffusion? *Angew. Chemie Int. Ed.* **59**, 19708–19715 (2020).

75. M. Thommes, K. Kaneko, A. V Neimark, J. P. Olivier, F. Rodriguez-Reinoso, J. Rouquerol, K. S. W. Sing, Physisorption of gases, with special reference to the evaluation of surface area and pore size distribution (IUPAC Technical Report). *Pure Appl. Chem.* **87**, 1051–1069 (2015).

76. P. Ferri, C. Li, C. Paris, A. Vidal-Moya, M. Moliner, M. Boronat, A. Corma, Chemical and Structural Parameter Connecting Cavity Architecture, Confined Hydrocarbon Pool Species, and MTO Product Selectivity in Small-Pore Cage-Based Zeolites. *ACS Catal.* **9**, 11542–11551 (2019).

77. R. J. Argauer, G. R. Landolt, Crystalline zeolite ZSM-5 and method for preparing the same. *US Pat. 3,702,886* (1969).

78. M. A. Camblor, A. Corma, L. A. Villaescusa, ITQ-4: a new large pore microporous polymorph of silica. *Chem. Commun.*, 749–750 (1997).

79. L. A. Villaescusa, P. A. Barrett, M. A. Camblor, ITQ-7: A New Pure Silica Polymorph with a Three-Dimensional System of Large Pore Channels. *Angew. Chemie Int. Ed.* **38**, 1997–2000 (1999).

80. C. T. Nimlos, A. J. Hoffman, Y. G. Hur, B. J. Lee, J. R. Di Iorio, D. D. Hibbitts, R. Gounder, Experimental and Theoretical Assessments of Aluminum Proximity in MFI Zeolites and Its Alteration by Organic and Inorganic Structure-Directing Agents. *Chem. Mater.* **32**, 9277–9298 (2020).

Acknowledgments:

The Electron Microscopy Service of the UPV is acknowledged for their help in sample characterization. Joaquín Martínez-Triguero and Chengeng Li are also acknowledged for helpful discussions on the MTO reaction. Ben Blaiszik is acknowledged for help with persistent data storage at the Materials Data Facility.

Funding: D.S.-K. and R.G.-B. acknowledge the Energy Initiative (MITEI) and MIT International Science and Technology Initiatives (MISTI) Seed Funds. D.S.-K. was additionally funded by the MIT Energy Fellowship. C.P., E.B.-J., M.M., and A.C. acknowledge financial support by the Spanish Government through the "Severo Ochoa" program (SEV-2016-0683, MINECO) and Grant RTI2018-101033-B-I00 (MCIU/AEI/FEDER, UE). E.B.-J. acknowledges the Spanish Government for an FPI scholarship (PRE2019-088360). Z.J., E.O., S.K., and Y.R.-L. acknowledge partial funding from the Designing Materials to Revolutionize and Engineer our Future (DMREF) from National Science Foundation (NSF), awards 1922311, 1922372, and 1922090, and the Office of Naval Research (ONR) under contract N00014-20-1-2280. S.K. was additionally funded by the Kwanjeong Educational Fellowship. Z.J. was also supported by the Department of Defense (DoD) through the National Defense Science Engineering Graduate (NDSEG) fellowship program. T. W. acknowledges financial support by the Swedish Research Council (Grant No. 2019-

05465). Computer calculations were executed at the Massachusetts Green High-Performance Computing Center with support from MIT Research Computing, and at the Extreme Science and Engineering Discovery Environment (XSEDE) (*53*) Expanse through allocation TG-DMR200068.

Author contributions: D.S.-K. designed and executed the simulations, computational analysis and software development. C.P. carried out the design and synthesis of the OSDAs. S.K. and E.B.-J. performed the synthesis and characterization of zeolites. E.B.-J. executed the MTO experiments. T.W. performed the TEM analysis of the **CHA**/**AEI** intergrowth and the simulation of the PXRD patterns of different **CHA**/**AEI** intergrown phases. Z.J. and E.O. provided the literature data. R.G.-B. conceived the project and supervised the computational research. M.M., Y.R.-L. and A.C. supervised the experimental research. D.S.-K., M.M., and R.G.-B. wrote the first manuscript draft. All authors contributed to the analysis of the data and to the final manuscript.

Competing interests: The authors are co-inventors of two patent applications based on the novel materials synthesized in this work.

Data and materials availability: The code used to automate the simulations of this work is available at https://doi.org/10.5281/zenodo.5260054 (*54*) and https://doi.org/10.5281/zenodo.5260056 (*55*). Literature data is available in Ref. (*19*). Results of atomistic simulations are available at the Materials Data Facility (*56*, *57*) through the accession code https://doi.org/10.18126/c5z9-zej7 (*58*). An interface to this data is available online at OSDB (https://zeodb.mit.edu/). The code and data used to produce all graphs in the manuscript are available at https://doi.org/10.5281/zenodo.5272354 (*59*). All other data needed to evaluate the conclusions of the paper are present in the paper or the Supplementary Materials.

Supplementary Materials:

Materials and Methods

Tables S1-S3

Figures S1-S25

Movie S1

References (60-80)

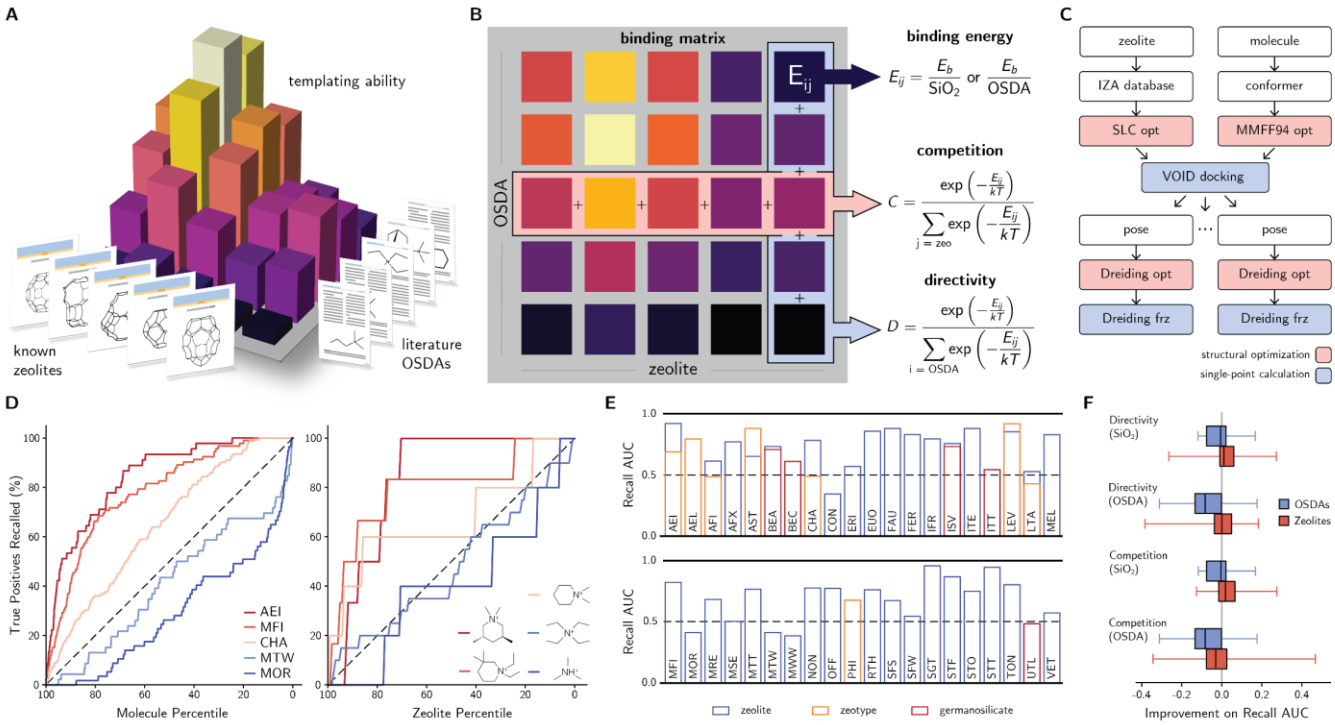

Figure 1: computational method used to quantify phase competition in zeolites.

A. OSDAs reported in the literature are docked into known zeolites, spanning a full matrix of binding energies.

B. Each element of the binding matrix is defined as the molecule-framework binding energy at the most favorable loading, normalized by the number of framework atoms or OSDA molecules (Methods). Along OSDAs, binding energies are ranked to determine how directive is a molecule toward a zeolite. Along zeolites, phase competition is quantified for a given OSDA.

C. Computational pipeline used to calculate binding energies for zeolite-OSDA pairs.

D. Explaining the literature with the templating energy. A recall curve is obtained by using the metric as a sorting algorithm for ranking OSDAs for a given zeolite (left) or zeolites for a given molecule (right). The dashed line indicates the expected recall curve for a random sorting algorithm.

E. Recall AUC for several zeolite frameworks according to their typical compositions.

F. Improvement of the recall AUC of OSDAs and zeolites using the proposed templating energy compared to other individual metrics. Including phase competition analysis improves the explanation of literature outcomes for about 70% of the zeolites in the literature.

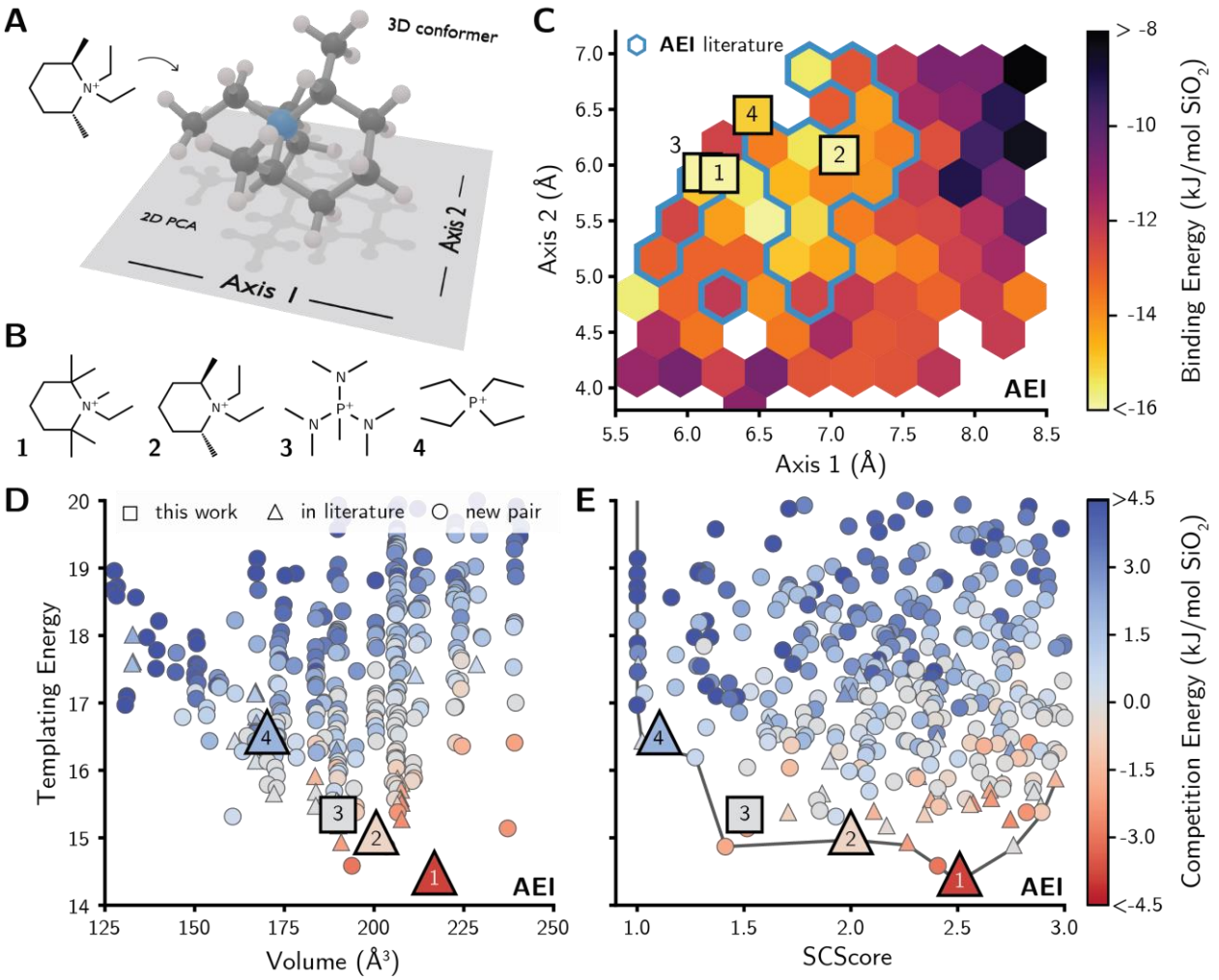

Figure 2: OSDA selectivity for **AEI** zeolite.

A. Schematic on the shape representation of OSDAs. The three-dimensional conformation is converted into two axes by projecting the atomic coordinates into a two-dimensional space using principal component analysis (PCA).

B. OSDAs candidates for the synthesis of **AEI**.

C. Relationship between the shapes of OSDAs and their binding energies toward **AEI**. The color of each hexagon indicates the mean competition energy for all OSDAs within that area. Blue outlines indicate that at least one OSDA within that region is known to synthesize **AEI** with zeolite composition.

D. Templating energy of OSDAs against their volume.

E. Templating energy of OSDAs against their SCScore. The Pareto frontier is shown with a solid gray line.

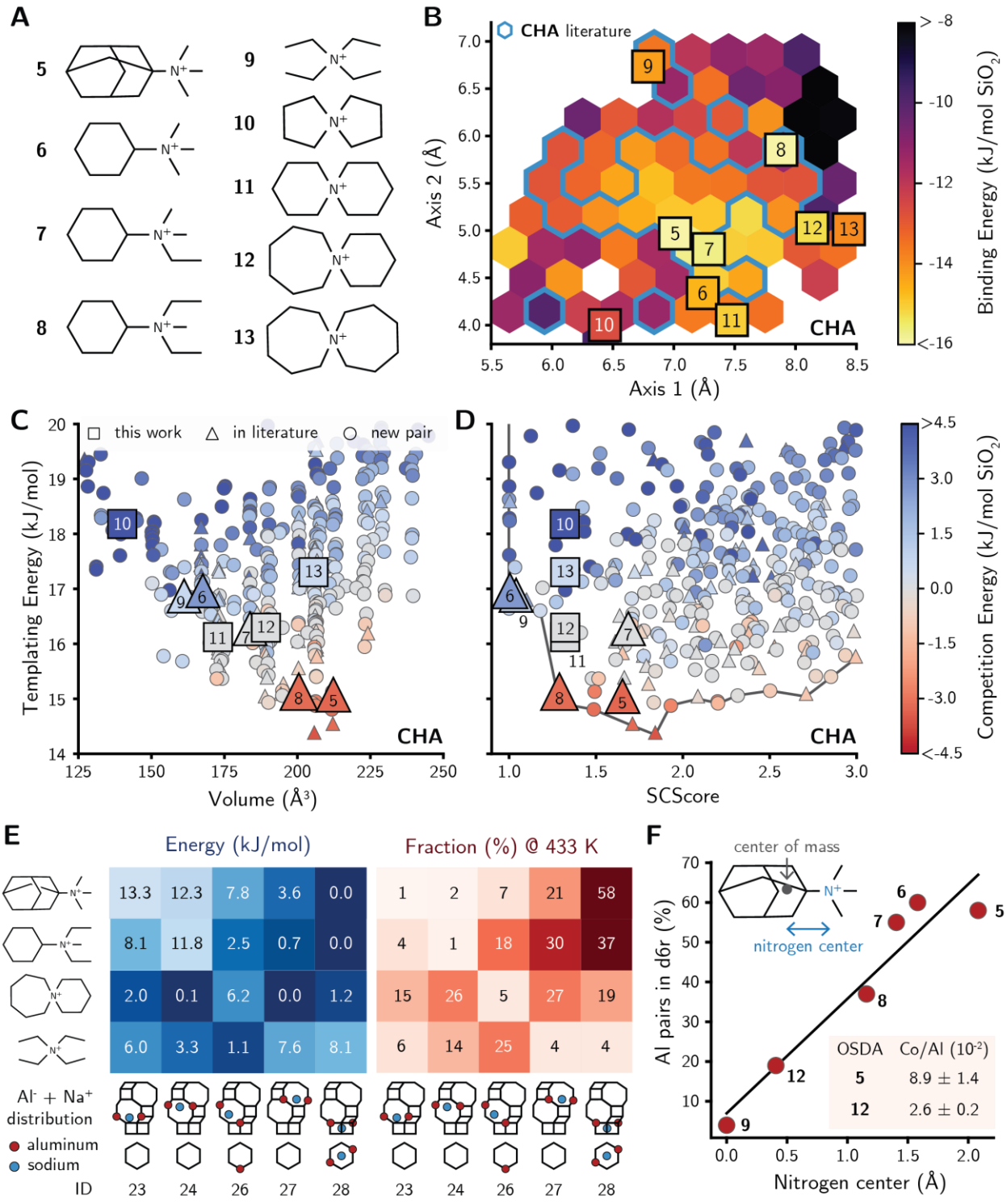

Figure 3: OSDA selectivity for **CHA** zeolite.

A. OSDAs candidates for the synthesis of **CHA**.

B. Relationship between the shapes of OSDAs and their binding energies toward **CHA**. The color of each hexagon indicates the mean competition energy for all OSDAs within that area. Blue outlines indicate that at least one OSDA within that region is known to synthesize **CHA** with zeolite composition.

C. Templating energy of OSDAs against their volume.
D. Templating energy of OSDAs against their SCScore. The Pareto frontier is shown with a solid gray line.
E. Influence of OSDA in the energy (blue) and fraction (red) of aluminum pairs in the cha cage in the presence of sodium. The predicted fraction of aluminum pairs is calculated at 433 K.
F. Relationship between the nitrogen center and the fraction of aluminum pairs in d6r units (distribution 28) for different OSDAs. Molecules with larger separation between the center of mass and the nitrogen center favor the pairing of aluminum atoms in the d6r units. The solid line is a linear regression of the data. Inset: Co/Al ratio from cobalt titration experiments for **CHA** samples synthesized with OSDAs **5** and **12**.

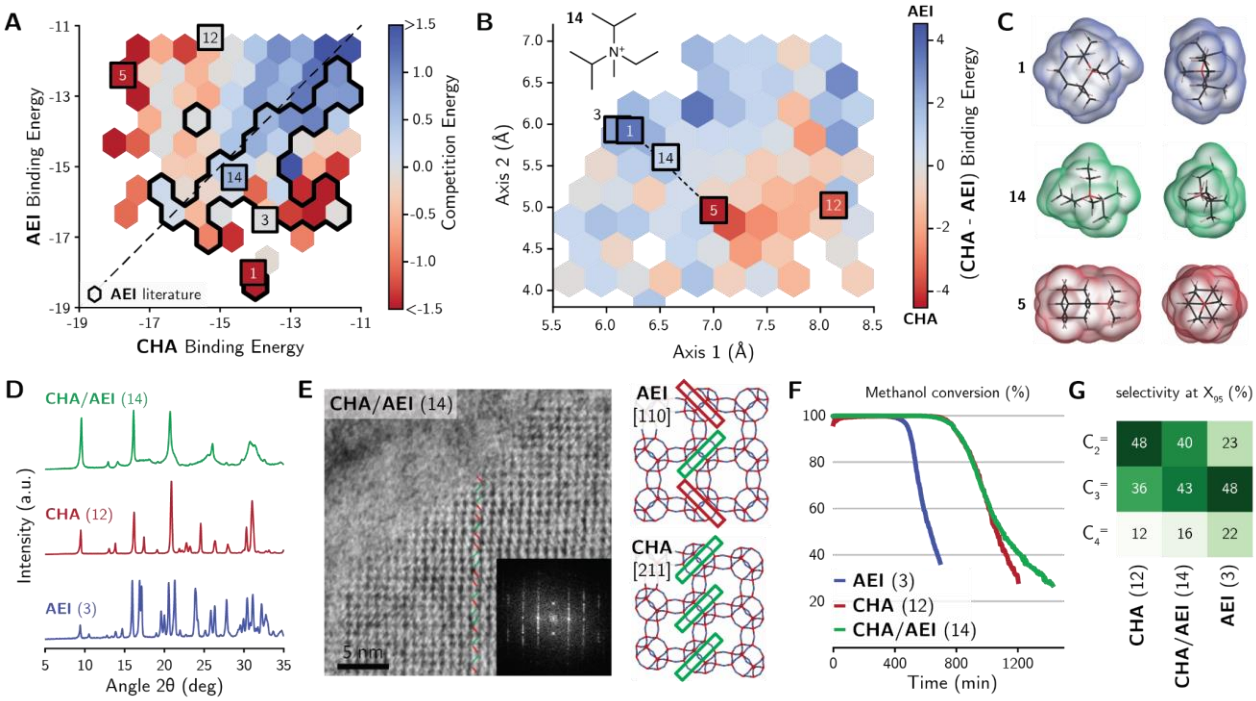

Figure 4: CHA/AEI intergrowth zeolite.

A. Comparison between binding energies of OSDAs in **CHA** and **AEI** zeolites. The color of each hexagon indicates the mean competition energy for all OSDAs within that area. All energies are given in kJ/mol SiO_2. Black outlines indicate that at least one OSDA within that region is known to synthesize **AEI** with zeolite composition.

B. Relationship between the shapes of OSDAs and their binding energies toward **CHA** or **AEI**. Colors shifted toward red (blue) indicate that the OSDA has a shape that favors the synthesis of **CHA** (**AEI**). OSDA **14**, the one that enables the **CHA**/**AEI** intergrowth, lies midway between the best OSDA for **AEI** (OSDA **1**) and the best OSDA for **CHA** (OSDA **5**). Energy difference given in kJ/mol SiO_2.

C. DFT-calculated charge densities for OSDAs **1**, **5** and **14**. OSDA **14** is in-between OSDAs **1** and **5** in terms of shape.

D. PXRD patterns of the as-prepared materials obtained with OSDAs **3** (**AEI**), **12** (**CHA**), and **14** (**CHA**/**AEI**).

E. iDPC-STEM image of **CHA**/**AEI** as synthesized by OSDA **14** acquired from a sample sectioned using ultramicrotomy, and structural models for **AEI** and **CHA** showing the stacking patterns seen in the STEM image. Inset: Fourier transform of the STEM image.

F. Comparison between methanol conversion profiles for **CHA**/**AEI** (OSDA **14**), **CHA** (OSDA **12**), and **AEI** (OSDA **3**).

G. Selectivity at X_{95} for **CHA** (OSDA **12**), **AEI** (OSDA **3**), and **CHA**/**AEI** (OSDA **14**). The selectivity of **CHA**/**AEI** (OSDA **14**) is between that of **CHA** (OSDA **12**) and **AEI** (OSDA **3**).

Supplementary Materials for: *A priori* control of zeolite phase competition and intergrowth with high-throughput simulations

Daniel Schwalbe-Koda, Soonhyoung Kwon, Cecilia Paris, Estefania Bello-Jurado, Zach Jensen, Elsa Olivetti, Tom Willhammar, Avelino Corma, Yuriy Román-Leshkov, Manuel Moliner*, Rafael Gómez-Bombarelli*

*Correspondence to: mmoliner@itq.upv.es, rafagb@mit.edu

This PDF file includes:

Materials and Methods
Tables S1 to S3
Figs. S1 to S25

Other Supplementary Materials for this manuscript include the following:

Movie S1

Materials and Methods

Theoretical Section

Force field calculations

Force field calculations were performed using the General Utility Lattice Program (GULP), version 5.1.1 (*60*, *61*), through the GULPy package (*21*). Initial zeolite structures were downloaded from the International Zeolite Association (IZA) database (*13*) and pre-optimized using the Sanders-Leslie-Catlow (SLC) parametrization (*62*). SMILES strings for OSDAs were extracted from the literature (*19*). Conformers for OSDAs were generated using RDKit (*63*) with the MMFF94 force field (*64*, *65*) after explicit enumeration of all stereoisomers for each molecule.

Generation of OSDA-zeolite poses was performed using the Voronoi and Monte Carlo docking algorithms as implemented in the VOID package (*20*). At most 5 different conformers for each OSDA are used as input guest geometries for VOID, depending on the molecular flexibility. Host structures pre-optimized with SLC were used as inputs for VOID. For certain zeolites with lattice parameters smaller than 10 Å in one direction, such as **MTW**, **MOR**, or **TON**, unit cells and 2x1x1 and 3x1x1 supercells (where the multiplying factor is applied in the direction of the short lattice parameter) were used as inputs for the docking package. The Voronoi docking algorithm used a threshold fitness function with minimum distance of 1.25 Å, 5 k-means clusters of Voronoi nodes generated with at least 3 Å of radius and probe radius of 0.1 Å. At first, docking is performed with the batch Voronoi docker parallelized over 20 images, and loading is increased until no more OSDAs can be added to the pose without overlap of molecules. If the procedure does not yield any poses, the docking job is repeated by parallelizing the batch docker over 100 images. If the Voronoi docker still does not lead to any images, the Monte Carlo docker algorithm is employed instead, and docking is attempted with 1,000 Monte Carlo steps with a normalized temperature of 0.1 for the first 500 steps and 0.0 for the remaining 500 steps. If no valid poses are generated after these three docking attempts are performed, the zeolite-OSDA pair is considered unfavorable, and no binding energies are calculated for them. Otherwise, we perform binding energy calculations for at least three OSDA loadings and report the one that minimizes the overall energy of the system (*20*, *21*).

The charge-neutral Dreiding force field (*66*) was used to model interactions between the pure-silica zeolite and the OSDA. Despite the role of aluminum distributions in zeolite synthesis, templating effects are mostly driven by dispersion interactions and can be reasonably simulated

using this approximation (*20*, *21*). Structural optimizations of poses were performed at constant volume using the conjugate gradient and rational function optimization algorithms, switching to the latter when the norm of the gradient dropped below 0.10 eV/Å. The frozen pose method was using for calculating the binding energies (*21*). A total of 586,303 poses were calculated for 112,426 complexes. 34,321 (~5.9%) of these poses had binding energy larger than zero due to unfavorable host-guest interactions and were removed from the binding matrix.

The total run time for successful structural optimizations with GULP was about 840,096 CPU-h, with an average time of 1.43 CPU-h per structural optimization. Successful docking jobs required about 14,676 CPU-h to be completed, averaging 0.14 CPU-h per docking job. 75% of the poses calculated had less than 372 atoms. A wall time of 3 days was imposed on all jobs for computational efficiency, preventing poses with thousands of atoms from running indefinitely.

Density Functional Theory calculations

Density Functional Theory (DFT) calculations were performed using the Vienna Ab-initio Simulation Package (VASP) (*67*, *68*), version 5.4.4, within the projector-augmented wave (PAW) method (*69*, *70*). The Perdew–Burke–Ernzerhof (PBE) functional within the generalized gradient approximation (GGA) (*71*) was used as the exchange-correlation functional. The kinetic energy cutoff for plane waves was restricted to 520 eV. A stopping criterion of 10^{-6} eV was adopted for the self-consistent field cycle energy convergence. Relaxation of atomic positions was performed until the Hellmann–Feynman forces on atoms were smaller than 10 meV/Å.

For the aluminum distributions in Fig. 3E, a 2x2x2 rhombohedral supercell of **CHA** was used, with one OSDA, one Na atom, and two aluminum sites (see details on Aluminum distribution sections below). For these systems, integrations over the Brillouin zone were performed using only the Gamma point. All structure relaxations were performed with variable unit cell sizes and shapes. For the OSDAs in Fig. 4C, integrations over the Brillouin zone were performed using only the Gamma point in a cubic box with a vacuum of 15 Å thickness in all directions to minimize interactions between periodic images. The isosurface of the plot was set to 0.0068 $e^-/Å^3$.

Binding energy metrics

Following structural optimizations at constant volume for poses, binding energies (E_b) between zeolites and OSDAs were calculated according to the frozen pose method (*21*),

$$E_b = E_p^{(\text{opt, V})} - E_h^{(\text{frz})} - \sum_i E_{g,i}^{(\text{frz})},$$

where $E_p^{(opt,V)}$ is the energy of the pose optimized at constant volume, $E_h^{(frz)}$ is the energy of the isolated host after removing the guests from that pose, and $E_{g,i}^{(frz)}$ is the energy of the guest *i* in the gas phase with the same geometry found in the optimized pose (*21*). Energies E_b can be normalized according to the number of OSDAs inside the zeolite cell (units of kJ/mol OSDA) or by the number of T sites in the zeolite framework (units of kJ/mol SiO_2). Since several poses are generated for each complex across different loadings and starting configurations, the binding energy of a zeolite-OSDA complex is defined as the minimum binding energy normalized by SiO_2 across all poses (*20*). The pose that minimizes this binding energy is taken as the most favorable one. Corresponding loadings and binding energies normalized by OSDA are reported according to this pose.

Binding energy metrics for a complex *(zeo, OSDA)* can be reported according to a directivity energy (E_d),

$$E_d^{(\text{zeo,OSDA})} = E_b^{(\text{zeo,OSDA})} - \min_{\text{mol}} E_b^{(\text{zeo,mol})},$$

which indicates how strong are the host-guest interactions of an OSDA with respect to the best OSDA for a given zeolite, or according to a competition energy (E_c),

$$E_c^{(\text{zeo,OSDA})} = E_b^{(\text{zeo,OSDA})} - \min_{\text{z}} E_b^{(\text{z,OSDA})},$$

indicating how favorable is a zeolite with respect to the best host for a given OSDA. It is often useful to represent the competition energies not in terms of the minimum, but the second energy minimum of the zeolites. This aids the intuition by providing a metric on how good is an OSDA for a given zeolite with respect to the second best one. With this notation, a good competition energy is as negative as possible. We use this notation for the competition energy on Figs. 2-4 of the main paper.

The previously shown energies can be normalized with a Boltzmann average,

$$D^{(\text{zeo,OSDA})} = \frac{\exp\left(\frac{-E_d^{(\text{zeo,OSDA})}}{kT}\right)}{\sum_{mol} \exp\left(\frac{-E_d^{(\text{zeo,mol})}}{kT}\right)},$$

and

$$C^{(\text{zeo,OSDA})} = \frac{\exp\left(\frac{-E_C^{(\text{zeo,OSDA})}}{kT}\right)}{\sum_z \exp\left(\frac{-E_C^{(\text{z,OSDA})}}{kT}\right)},$$

with *k* the Boltzmann constant and *T* a temperature. The normalization quantifies how accessible is a given zeolite-OSDA pair with respect to all others possible zeolite-OSDA pairs. Since binding energies can be normalized either by SiO_2 or OSDA, it is often adequate to normalize the binding energy per OSDA in terms of the number of atoms of each OSDA, which forces both normalizations to be around the same range of energies. Then, the templating energy (E_T) is constructed from the geometric mean of these contributions normalized by each of these quantities,

$$E_T = -kT \log(C_{\text{OSDA}} D_{\text{OSDA}} C_{\text{SiO2}} D_{\text{SiO2}})^{1/4}.$$

The templating energy is minimized by simultaneously minimizing the directivity and the competition energies of the zeolite-OSDA pair. We adopt T = 400 K as an approximation to hydrothermal temperatures during the synthesis of zeolites. Small changes in this parameter do not significantly affect the overall ranking of zeolite-OSDA pairs. The templating energy was calculated only for OSDAs docked in at least five different frameworks to ensure a reasonable distribution of competition energies.

Literature recall

Recall from the literature is calculated by sorting all the calculated zeolite-OSDA pairs along either a zeolite or OSDA according to a binding energy metric. The recall curve is then constructed by plotting the cumulative percentage of true positives recalled from the literature with respect to their percentile (Fig. S4). The recall area under the curve (AUC) is normalized by the AUC of the best case scenario, in which all positive zeolite-OSDA pairs along a series are ranked as the best pairs. The expected AUC for a random sorting is 0.5, as each ranking with AUC *p* has an inverted ranking with AUC *(1-p)*. Only zeolites synthesized from at least 10 different OSDAs were selected to calculate the recall AUC. Conversely, only OSDAs crystallizing at least 6 different zeolite frameworks were considered when plotting the recall AUC. Different stereoisomers of OSDAs are treated as different molecules. Whenever the literature data does not specify a stereoisomer, we consider all stereoisomers as positive ligands for the zeolite under study. Overall, this approximation should decrease the AUC if different stereoisomers have a large influence in the synthesis of the zeolite.

Physical descriptors from OSDAs

Synthetic complexity of OSDAs is quantified through the SCScore, proposed by Coley *et al*. (*30*). It uses a neural network-based model to estimate the complexity of a molecule after being trained on 12 million reactions. We used a Morgan fingerprint of length 1024 bits for input molecules, and the weights of the pretrained model published as `model.ckpt-10654.as_numpy.json.gz` at https://github.com/connorcoley/scscore (commit 37090a6).

OSDA volume is calculated by using a grid-encoding of the molecular shape using a grid spacing of 0.2 Å and 2.0 Å of margin for the boxes, as implemented in RDKit (*63*). The ground state geometry for each molecule is used as input for calculating the volume.

Two-dimensional (2D) shape descriptors were calculated by projecting the atomic coordinates into a 2D space based on a principal component analysis (PCA) of the positions. The range of the distribution of points in each principal component is reported as the axis of the conformer. Axis 1 is reported as the larger axis, whereas Axis 2 is the smaller axis (Fig. 2B).

For monocationic OSDAs, the nitrogen center was computed by taking the distance between the nitrogen atom and the center of the mass of the molecule. This rationale can be used for OSDAs with other charged atoms, such as phosphorus. No OSDAs with charge different than +1 were considered in the screening shown in Fig. S14.

OSDB

The database containing all results and literature data was created using PostgreSQL and interfaced with Python through psycopg2. Django was used as the object-relation manager and web framework. Page templates were written in HTML.

Aluminum distributions in **CHA**

Energies of aluminum pairs in *cha* cages occluded with sodium and different OSDAs were computed using DFT calculations (see Density Functional Theory section). A 2x2x2 rhombohedral **CHA** supercell was used in all calculations. Only one Na^+ and OSDA were added to the supercell, thus minimizing the effects of periodic boundary conditions in the aluminum distributions. The

supercells and enumeration of aluminum pairs (Fig. S18) follow the notation proposed in (*43*). The energy of each pair is given with respect to the most stable aluminum pair per OSDA. Since the OSDAs are asymmetrical, only the most stable arrangement per OSDA was calculated, i.e. with the nitrogen atom closest to the *d6r* unit containing the aluminum pairs or the sodium ion (*43*).

The fraction f_i of each arrangement expected at the synthesis conditions is estimated by the Boltzmann probability that a pair i with energy E_i will be present at the temperature T,

$$f_i = \frac{\exp\left(\frac{-E_i}{kT}\right)}{\sum_j \exp\left(\frac{-E_j}{kT}\right)},$$

where k is the Boltzmann constant. The fraction of each aluminum pairing in **CHA** is estimated at 433 K, the approximate temperature of the synthesis. Although the simulations take into account a single Al pair (Si/Al =15 in an isolated *cha* cage), the energetics are able to quantify the bias of each OSDA in directing aluminum pairs to specific locations of the *cha* cage and may be generalizable to lower Si/Al ratios. Simulations with lower Si/Al ratios, i.e. with more than one Na^+ ion per cage, are prohibitively expensive with DFT calculations, as the number of unique Al and Na^+ placements grows exponentially larger.

Protonated forms of the *cha* cage were computed by placing hydrogen atoms in oxygens atoms adjacent to aluminum sites and performing full structural optimizations using DFT. The protonated oxygens sites were selected in order to maximize the distance between hydrogen atoms, thus reducing possible H-H overlaps and minimizing the number of calculations required per aluminum distribution. Although adding water to the simulations can influence the stability of aluminum pairs (*72*), we simulate the cha cage under anhydrous conditions as a simplified reference for non-OSDA-biased aluminum distributions.

Simulated PXRD pattern for **CHA**/**AEI** intergrowth

Simulated powder X-ray diffraction (PXRD) patterns were obtained using the general recursion method implemented in DIFFaX (*73*). A model representing an intergrowth of the **CHA** and **AEI** structures was constructed. The probabilities for each of the structures were varied to obtain PXRD patterns of different fractions of the two structures. The peak shape parameters for the Pseudo Voigt function were set to 0.89, –0.32, 0.08 for U, V, W respectively.

Experimental Section

1.- Synthesis of the organic structure-directing agents (OSDA)

1.1- Synthesis of tris(dimethylamino)(methyl)phosphonium hydroxide (OSDA **3**)

The reaction must be performed under dry conditions: oven-dried glassware materials, anhydrous deoxygenated solvents and inert atmosphere (argon). 0.149 moles of tris-(dimethylamino)-phosphine (24.23 g), previously cold at fridge temperature (4-5°C), was added by transfer to a two-necked flask equipped with a condenser and argon flux. Then, it was dissolved with 200 ml of anhydrous tetrahydrofuran and the resulting solution was cold in an ice-bath. Under stirring, an excess of methyl iodide (0.223 moles, 31.62 g) was added dropwise, and once the mixture reached room temperature, it was left to react for 24 h. A white precipitate was formed that was isolated by filtration, washed with diethyl ether and dried under vacuum and heating, and stored under inert atmosphere.

50.0 mmol of the iodide form of the template was dissolved in 110 ml of water. Then, 100 g of anion-exchange resin (Amberlite IRN-78) was added to the solution and kept under stir for 24 hours. Finally, the solution was collected by filtration and the obtained hydroxide form of template has an exchange efficiency of at least 95%.

1.2- Synthesis of tetraethylphosphonium hydroxide (OSDA **4**)

Tetraethylphosphonium bromide (ABCR, 95%) was used as purchased, without further purification. 50.0 mmol of the bromide form of the template was dissolved in 110 ml of water. Then, 100 g of anion-exchange resin (Amberlite IRN-78) was added to the solution and kept under stir for 24 hours. Finally, the solution was collected by filtration and the obtained hydroxide form of template has an exchange efficiency of at least 95%.

1.3- Synthesis of N,N,N-trimethylcyclohexanaminium hydroxide (OSDA **6**)

A solution of *N*,*N*-dimethylcyclohexylamine (42.45g; 0.33 moles) in chloroform (600 ml) was transfer to a two-neck round flask, equipped with a condenser and stirrer, and cold to 0 ºC with an ice bath. Then, under strong stirring, iodomethane (141,94 g; 1 mol) was added dropwise. When the solution reached room temperature, it was left to react for 48h. The solvent was removed by distillation under reduced pressure (rotavap) until a residue was formed. 500 ml of ethyl acetate was poured to the residue, for product precipitation. The solid was isolated by filtration, washed

with diethyl ether and finally dried under reduced pressure and heating. The solid was stored under inert atmosphere.

50.0 mmol of the iodide form of the template was dissolved in 110 ml of water. Then, 100 g of anion-exchange resin (Amberlite IRN-78) was added to the solution and kept under stir for 24 hours. Finally, the solution was collected by filtration and the obtained hydroxide form of template has an exchange efficiency of at least 95%.

1.4- Synthesis of N,N-dimethyl-N-ethylcyclohexanaminium hydroxide (OSDA **7**)

0.50 moles of iodoethane (77,98 g) is added dropwise and under stirring to a solution of *N*,*N*-dimethylcyclohexylamine (31.81 g; 0.25 mol) in ethanol (200 ml). The resulting mixture is allowed to react at room temperature over one hour. Then, once the solution is stabilized, is slowly warmed up to 50 ºC and left to react for 72h. When the reaction reached room temperature, a solution of ethyl acetate-diethyl ether is added and a white precipitate is formed. The product is isolated by filtration and finally, dried under vacuum and heating.

50.0 mmol of the iodide form of the template was dissolved in 110 ml of water. Then, 100 g of anion-exchange resin (Amberlite IRN-78) was added to the solution and kept under stir for 24 hours. Finally, the solution was collected by filtration and the obtained hydroxide form of template has an exchange efficiency of at least 95%.

1.5- Synthesis of N,N-diethyl-N-methylcyclohexanaminium hydroxide (OSDA **8**)

The reaction is performed under very dried synthesis conditions. *N*,*N*-diethylcyclohexylamine (48.89 g; 0.315 moles) is dissolved in methanol anhydrous (150 ml) under argon atmosphere. The resulting solution is cold in an ice-acetone bath, and then under strong stirring an excess of iodomethane is slowly added. When the solution reached room temperature, the crude is allowed to react for 72 h. Once the reaction is complete, the product is rapidly isolated by filtration under vacuum and argon atmosphere. Finally, the white precipitate obtained is dried under vacuum and heating, and stored in an inert atmosphere.

50.0 mmol of the iodide form of the template was dissolved in 110 ml of water. Then, 100 g of anion-exchange resin (Amberlite IRN-78) was added to the solution and kept under stir for 24 hours. Finally, the solution was collected by filtration and the obtained hydroxide form of template has an exchange efficiency of at least 95%.

1.6.- Synthesis of azaspiro[4.4] hydroxide (OSDA **10**)

Pyrrolidine (17.78 g; 0.25 moles) was dissolved in acetonitrile (200 ml), and the solution transferred to a two-neck round flask provided with a stirrer and condenser. Potassium carbonate (27.64 g, 0.20 moles) was added under stirring and the suspension left to react one hour at room temperature. Then, 1,4-dibromobutane (53.98 g; 0.25 moles) was added and the crude slowly heated until reaching reflux temperature (90 ºC). The crude was left to react for 48 h. Once the reaction finished, the solvent was removed by evaporation and the residue obtained dissolved in chloroform. The inorganic salts were removed by filtration and the organic phase was reserved. The chloroform was removed under vacuum and the product crystallized by addition of a mixture of ethyl acetate-acetone. Finally, the product was dried under reduced pressure and heating, and stored in an inert atmosphere.

50.0 mmol of the bromide form of the template was dissolved in 110 ml of water. Then, 100 g of anion-exchange resin (Amberlite IRN-78) was added to the solution and kept under stir for 24 hours. Finally, the solution was collected by filtration and the obtained hydroxide form of template has an exchange efficiency of at least 90%.

1.7.- Synthesis of azaspiro[5.5] hydroxide (OSDA **11**)

Piperidine (21.28 g; 0.25 moles) was dissolved in acetonitrile (200 ml), and the solution transferred to a two-neck round flask provided with a stirrer and condenser. Potassium carbonate (27.64 g, 0.20 moles) was added under stirring and the suspension left to react one hour at room temperature. Then, 1,5-dibromopentane (57.48 g; 0.25 moles) was added and the crude slowly heated until reaching reflux temperature (90 ºC). The crude was kept under reflux for 48 h. Then, the acetonitrile was removed by evaporation and the resulting crude, was dissolved in chloroform. The inorganic salts were removed by filtration and the organic phase was reserved. The chloroform was removed under vacuum and the product crystallized by addition of a mixture of ethyl acetate-acetone. Purification by recrystallization was done by dissolution in methanol followed by precipitation with ethyl acetate-acetone solution. Finally, the product was isolated and dried under reduced pressure and heating, and stored in an inert atmosphere.

50.0 mmol of the bromide form of the template was dissolved in 110 ml of water. Then, 100 g of anion-exchange resin (Amberlite IRN-78) was added to the solution and kept under stir for 24

hours. Finally, the solution was collected by filtration and the obtained hydroxide form of template has an exchange efficiency of at least 90%.

1.8.- Synthesis of 6-azaspiro[5.6]dodecan-6-ium hydroxide (OSDA **12**)

The followed synthetic route is a modification of the synthesis described by Millini et al. (*42*). 0.188 moles of 1,5-dibromopentane (TCI Chemical, 98%, 43.22g), is added to a 500mL two-necked round flask connected with a condenser. Since the reaction is very exothermic, the solution was cooled using ice bath. Then, aqueous ammonium hydroxide solution (Sigma-Aldrich, 28 wt%, 120 g) was added in small portions and under constant stirring. Under vigorous stirring, 0.188 moles of hexamethyleneimine (Acros Organics, 99%, 18.64 g) was added dropwise for 20 minutes. The resulting mixture was left to reach room temperature, and then slowly heated until reflux temperature (120 °C). A second aliquot of ammonium hydroxide solution (Sigma-Aldrich, 28 wt%, 60 g) was added dropwise during the reflux. When a clear yellow solution was observed, the reaction mixture was left 4 h at this temperature. After the reaction finished, and the mixture cold to room temperature, the solvent was completely removed by rotary evaporation, and the 6-azaspiro[5.6]dodecan-6-ium bromide was obtained as a white precipitate. Finally, it was crystalized using anhydrous 2-propanol and further washed with chloroform. The product was isolated by filtration, dried under vacuum and heating, and stored under inert atmosphere.

50.0 mmol of the bromide form of the template was dissolved in 110 ml of water. Then, 100 g of anion-exchange resin (Amberlite IRN-78) was added to the solution and kept under stir for 24 hours. Finally, the solution was collected by filtration and the obtained hydroxide form of template has an exchange efficiency of at least 95%. The solution was concentrated using rotary evaporator. The final concentration of the OSDA **12** solution was titrated with 0.01N HCl solution.

1.9.- Synthesis of 7-azaspiro[6.6]tridecan-7-ium hydroxide (OSDA **13**)

0.3 moles of 1,6-dibromohexane (TCI Chemical, 98%, 74.68g), is added to a 500mL two-necked round flask connected with a condenser. Since the reaction is exothermic, the solution was cooled using ice bath. Then, aqueous ammonium hydroxide solution (Sigma-Aldrich, 28 wt%, 188 g) was added in small portions and under constant stirring. Under vigorous stirring, 0.3 moles of hexamethyleneimine (Acros Organics, 99%, 29.75 g) was added dropwise for 30 minutes. The resulting mixture was left to reach room temperature, and then slowly heated until reflux

temperature (120 °C). A second aliquot of ammonium hydroxide solution (Sigma-Aldrich, 28 wt%, 94 g) was added dropwise during the reflux. After the color of the solution turned to brown, the reaction mixture was left 4 h at this temperature. When the reaction finished, and the mixture cold to room temperature, the solvent was completely removed by rotary evaporation, and the 7-azaspiro[6.6]tridecan-7-ium bromide was obtained as a white precipitate. Finally, it was crystalized using anhydrous 2-propanol and further washed with chloroform, hexane and acetone. The product was isolated by filtration, dried under vacuum and heating, and stored under inert atmosphere.

50.0 mmol of the bromide form of the template was dissolved in 110 ml of water. Then, 100 g of anion-exchange resin (Amberlite IRN-78) was added to the solution and kept under stir for 24 hours. Finally, the solution was collected by filtration and the obtained hydroxide form of template has an exchange efficiency of at least 95%. The solution was concentrated using rotary evaporator. The final concentration of the OSDA **13** solution was titrated with 0.01N HCl solution.

1.10.- Synthesis of N-ethyl-N-methyl-diisopropyl-ammonium hydroxide (OSDA **14**)

In a round-bottom flask, 0.278 moles of N-ethyl-diisopropylamine (35.94 g) is dissolved in 150 ml of diethyl ether. The resulting solution is cold in an ice-bath and under continuous stirring, and 0.707 moles of methyl iodide (100.32 g) is added dropwise in three aliquots over a 24 h period. Then, the solution is left to react one week at room temperature under stirring. When the reaction is completed, the N-ethyl-N-methyl-diisopropyl-ammonium iodide precipitate as a white solid. The product is isolated by filtration and dried.

50.0 mmol of the iodide form of the template was dissolved in 110 ml of water. Then, 100 g of anion-exchange resin (Amberlite IRN-78) was added to the solution and kept under stir for 24 hours. Finally, the solution was collected by filtration and the obtained hydroxide form of template has an exchange efficiency of at least 95%.

2.- Synthesis of zeolites

2.1.- Synthesis of **AEI** zeolites

2.1.1.- Synthesis of the **AEI** (OSDA **3**) zeolite using CBV720 as Si-Al source

1.78 g of **FAU** zeolite (**FAU**, CBV720 with Si/Al=14, Zeolyst, Lot number: 72004003128) was added to 19.28 g of a 7.6 wt% aqueous solution of OSDA **3**. The mixture was stirred for 10 minutes

for homogenization. Afterwards, 1.02 g of a 20 wt% aqueous solution of sodium hydroxide was added, and the synthesis mixture was maintained under stirring the required time to evaporate the excess of water until achieving the desired gel concentration. The final gel composition was: SiO_2 : 0.036 Al_2O_3 : 0.3 OSDA **3** : 0.2 NaOH : 15 H_2O.

The resultant gel was charged into a stainless steel autoclave with a Teflon liner. The crystallization was then conducted at 135 °C for 7 days under dynamic conditions. The solid product was filtered, washed with abundant water, and dried at 100 °C. The solids were calcined at 800 °C for 4 h in hydrogen to remove the occluded organic molecules (special care should be taken to the toxic PH_3 generated during this process). After cooled to room temperature, the solids were calcined at 580 °C for 5 h in air.

2.1.2.- Synthesis of the **AEI** (std) zeolite using CBV720 as Si-Al source

The syntheses of N,N-dimethyl-3,5-dimethylpiperidinium (DMP) and the corresponding **AEI** zeolite using DMP as OSDA have been described in (*74*).

2.1.3.- General synthesis procedure to attempt the synthesis of **AEI** with different OSDAs and Si-Al sources

In a typical synthesis procedure, an aqueous solution of the organic template (OSDA **3** or OSDA **4**) in its hydroxide form was firstly mixed with the proper amount of water and sodium hydroxide. Secondly, the required amount of precrystallized low-cost Al-rich **FAU** zeolite (CBV500, Zeolyst) and amorphous silica (fumed silica, Aldrich, Lot# SLCC7341) sources were added to the above mixture. The synthesis mixture was maintained under stirring the required time to evaporate the excess of water until achieving the desired gel concentration. The final gel composition would be 1 SiO_2 : 0.045-0.062 Al_2O_3 : 0.2 OSDA : 0.25 NaOH : 5 H_2O. The gel was then introduced into a Teflon-lined stainless autoclave. The crystallization was then conducted at 135 °C for 7 days under static conditions. The synthesis conditions employed for the different silicoaluminates are summarized in Fig. S9. After the crystallization procedure, the solids were filtered and washed with abundant distilled water and dried at 100 °C overnight.

2.2.- Synthesis of **CHA** zeolites

2.2.1.- Synthesis of the **CHA** (OSDA **12**) zeolite using CBV720 as Si-Al source

0.53 g of **FAU** zeolite (**FAU**, CBV720 with Si/Al=14, Zeolyst, Lot number: 72004003128) was added to 4.56 g of a 6.1 wt% aqueous solution of OSDA5. The mixture was stirred for 10 minutes for homogenization. Afterwards, 0.45 g of a 20 wt% aqueous solution of sodium hydroxide was added, and the synthesis mixture was maintained under stirring the required time to evaporate the excess of water until achieving the desired gel concentration.

The final gel composition was: 1 SiO_2 : 0.036 Al_2O_3 : 0.2 OSDA **12** : 0.3 NaOH : 15 H_2O.

The resultant gel was charged into a stainless steel autoclave with a Teflon liner. The crystallization was then conducted at 150 °C for 12 days under dynamic conditions. The solid product was filtered, washed with abundant water, and dried at 100 °C. The solids were calcined at 580 °C for 5 h in air to remove the occluded organic molecules.

2.2.2.- Synthesis of the **CHA** (std) zeolite using CBV720 as Si-Al source

3.79 g of **FAU** zeolite (**FAU**, CBV720 with Si/Al=14, Zeolyst, Lot number: 72004003128) was added to 15.27 g of a 25 wt% aqueous solution of N,N,N-trimethyl-1-adamantylammonium hydroxide (TMAda, Sachem). The mixture was stirred for 10 minutes for homogenization. Afterwards, 2.42 g of a 20 wt% aqueous solution of sodium hydroxide was added, and the synthesis mixture was maintained under stirring the required time to evaporate the excess of water until achieving the desired gel concentration. The final gel composition was: SiO_2 : 0.036 Al_2O_3 : 0.3 TMAda : 0.2 NaOH : 15 H_2O.

The resultant gel was charged into a stainless steel autoclave with a Teflon liner. The crystallization was then conducted at 160 °C for 10 days under dynamic conditions. The solid product was filtered, washed with abundant water, and dried at 100 °C. The solids were calcined at 580 °C for 5 h in air to remove the occluded organic molecules.

2.2.3.- General synthesis procedure to attempt the synthesis of **CHA** with different OSDAs and Si-Al sources

- *Using pre-crystallized FAU sources as the single Si-Al source*

In a typical synthesis procedure, an aqueous solution of the organic template (OSDA **6**, **7**, **8, 10**, **11**, **12** or **13**) in its hydroxide form was firstly mixed with the proper amount of water and sodium hydroxide or potassium hydroxide (if required). Secondly, the required amount of precrystallized **FAU** zeolites [CBV712 (Si/Al~6), CBV720 (Si/Al~15) or CBV760 (Si/Al~26), Zeolyst] was

added to the above mixture. The synthesis mixture was maintained under stirring the required time to evaporate the excess of water until achieving the desired gel concentration. The final gel composition would be 1 SiO_2 : 0.019-0.083 Al_2O_3 : 0.3 OSDA : 0-0.4 NaOH : 0-0.4 KOH : 15 H_2O. The gel was then introduced into a Teflon-lined stainless autoclave. The crystallization was conducted at 150-175 °C in static conditions for 5-10 days. The synthesis conditions of the different silicoaluminate zeolites are summarized in Fig. S11A and S16A,B,F. After the crystallization procedure, the solids were filtered and washed with abundant distilled water and dried at 100 °C overnight.

- *Using pre-crystallized low-cost Al-rich **FAU** (CBV500) as Al source and amorphous silica as Si source*

In a typical synthesis procedure, an aqueous solution of the organic template (OSDA **6**, **7**, **8** or **12**) in its hydroxide form was firstly mixed with the proper amount of water and sodium hydroxide (if required). Secondly, the required amount of precrystallized low-cost Al-rich FAU zeolite (CBV500, Zeolyst) as Al source and amorphous silica (fumed silica, Aldrich, Lot# SLCC7341; or colloidal silica suspension, Ludox AS40, Sigma-Aldrich) sources were added to the above mixture. The synthesis mixture was maintained under stirring the required time to evaporate the excess of water until achieving the desired gel concentration. The final gel composition would be SiO_2 / 0.02-0.062 Al_2O_3 / 0.22-0.3 OSDA / 0-0.4 NaOH / 15 H_2O. The gel was then introduced into a Teflon-lined stainless autoclave. The crystallization was conducted at 135-150 °C in static conditions for 7-12 days. The synthesis conditions of the different aluminosilicate materials are summarized in Fig. S11B and S16D. After the crystallization procedure, the solids were filtered and washed with abundant distilled water and dried at 100 °C overnight.

- *Using amorphous precursors as Si and Al sources*

In a typical synthesis procedure, an aqueous solution of the organic template (OSDA **6**, **7**, **8** or **12**) in its hydroxide form was firstly mixed with the proper amount of water and sodium hydroxide (if required). Secondly, the required amount of the Al amorphous source (aluminum hydroxide, Alfa-Aesar) and amorphous silica (fumed silica, Aldrich, Lot# SLCC7341; or colloidal silica suspension, Ludox HS40, Sigma-Aldrich) sources were added to the above mixture. If required, 10%wt **CHA** seeds were added in the synthesis gel. The synthesis mixture was maintained under

stirring the required time to evaporate the excess of water until achieving the desired gel concentration. The final gel composition would be 1 SiO_2 : 0.02-0.083 Al_2O_3 : 0.3 OSDA : 0-0.4 NaOH : 5-15 H_2O. The gel was then introduced into a Teflon-lined stainless autoclave. The crystallization was conducted at 135-175 °C in static conditions for 7-12 days. The synthesis conditions of the different aluminosilicate materials are summarized in Fig. S11C,D,E and S16C,E. After the crystallization procedure, the solids were filtered and washed with abundant distilled water and dried at 100°C overnight.

2.3.- Synthesis of **CHA/AEI** zeolite

2.3.1.- Synthesis of the **CHA**/**AEI** (OSDA **14**) zeolite

1.43 g of **FAU** zeolite (**FAU**, CBV720 with Si/Al=14, Zeolyst, Lot number: 72004003128) was added to 10.34 g of a 9.37 wt% aqueous solution of OSDA **14**. The mixture was stirred for 10 minutes for homogenization. Afterwards, 0.41 g of a 40 wt% aqueous solution of sodium hydroxide was added, and the synthesis mixture was maintained under stirring the required time to evaporate the excess of water until achieving the desired gel concentration. The final gel composition was: SiO_2 : 0.036 Al_2O_3 : 0.3 OSDA **14** : 0.2 NaOH : 15 H_2O.

The resultant gel was charged into a stainless steel autoclave with a Teflon liner. The crystallization was then conducted at 140 °C for 5 days under dynamic conditions. The solid product was filtered, washed with abundant water, and dried at 100 °C. The solids were calcined at 580 °C for 5 h in air to remove the occluded organic molecules.

3.- Characterization

PXRD measurements

Powder X-ray diffraction (PXRD) measurements were performed with a multi sample Philips X'Pert diffractometer equipped with a graphite monochromator, operating at 45 kV and 40 mA, and using Cu Kα radiation (λ = 0.1542 nm).

ICP analyses

Chemical analyses were carried out in a Varian 715-ES ICP-Optical Emission spectrometer, after solid dissolution in HNO_3/HCl/HF aqueous solution. The organic content of the as-made materials was determined by elemental analysis performed on a SCHN FISONS elemental analyzer.

Microscopy

The morphology of the samples was studied by field emission scanning electron microscopy (FESEM) using a ZEISS Ultra-55 microscope.

The sample was prepared for transmission electron microscopy (TEM) studies using ultra microtomy in order to obtain thin sections and to access the desired crystallographic direction for imaging. The zeolite powder was dried in oven overnight and embedded in an epoxy resin (Agar Low Viscosity Resin) which was hardened at 60 °C for 24 h. Sectioning was performed using a Leica Ultracut UCT to an estimated thickness of 50 nm. Scanning transmission electron microscopy (STEM) images were obtained using a ThermoFisher ThemisZ double aberration-corrected TEM operated at an accelerating voltage of 300 kV. The contrast was formed using integrated differential phase contrast (iDPC). A high-pass filter was applied to the iDPC images in order to reduce low frequency features. The STEM images were acquired using an electron beam current of 24 pA, a convergence angle of 16 mrad and a dwell time of 10 µs. The sample was dried in vacuum at 180ºC during 3h prior to data acquisition in order to remove adsorbed water and enhance stability.

Textural analysis

The textural analysis was performed by measuring N_2 isotherms at 77 K on volumetric Micromeritics ASAP 2020 device after activation at 400 °C and under vacuum. The Brunauer-Emmet-Teller (BET) and t-plot methods were used in order to obtain estimations of the surface area and the micropore volume, respectively (*75*).

NMR

Solid-state MAS NMR spectra were recorded with a Bruker AV400 III HD spectrometer. ^{27}Al MAS NMR spectra were recorded at 104.2 MHz with a spinning rate of 10 kHz and a 90° pulse length of 0.5 µs with 1 s repetition time. ^{13}C MAS NNR spectra were recorded at spinning rate of 15 kHz with a 90° pulse length of 5 us using high-power proton decoupling (spinal64) µs with 20 s repetition time. ^{31}P MAS NMR spectra were recorded at 161.9 MHz with a spinning rate of 10 kHz, a $\pi/2$ pulse of 5 µs with 20 s repetition time. ^{27}Al, ^{13}C and ^{31}P chemical shifts were referenced to $Al^{3+}(H_2O)_6$, adamantane, and 85% H_3PO_4, respectively.

Cobalt titration experiments

Zeolites were converted to their H^+ form by ion-exchanging under aqueous solution using 1 M NH_4NO_3 solution (Sigma-Aldrich, 99.9%) for 24 h in ambient conditions. The ion-exchanged zeolites were centrifuged and washed with deionized water three times. After drying at 373 K oven under stagnant air for 24 h, the zeolites were converted to their H^+ form by calcining in flowing dry air (Airgas, dry air CGA-590) at 755 K for 6 hours.

Co^{2+} form with ion-exchange under aqueous solution using 150 cm^3 of 0.5 M $Co(NO_3)_2$ (Sigma-Aldrich, hexahydrate form, 99%) solution per grams of zeolites for 12 h at ambient condition under stirring. After the exchange, the samples were washed with deionized water four times, recovered using centrifugation, and dried at 373 K under stagnant air for 24 h. To remove nitrates, the ion-exchanged zeolites were calcined in flowing dry air (Airgas, dry air CGA-590) at 755 K for 6 hours.

In order to measure how much cobalt has been loaded in the zeolite framework, 5 to 10 mg of zeolites have been dissolved in 100 uL of concentrated HF solution (Sigma-Aldrich, 48%) for 4 hours, followed by diluting the solution with 2% nitric acid (diluted from Sigma-Aldrich, 70%). The solution was vortexed at 3000 rpm for 1 minute to make homogeneous solution. Cobalt (Co), sodium (Na), aluminum (Al), and silicon (Si) contents were determined using inductively coupled plasma optical emission spectroscopy (ICP-OES) (Agilent 7900). 10.0 mg of zeolite were placed in a polyethylene microfuge tube (1.5 mL) and digested in 0.1mL hydrofluoric acid (48 wt %, trace metals basis, Sigma-Aldrich) for 3 h. The hydrofluoric acid solution was diluted to a total mass of 10.0 g using 2 wt % aqueous nitric acid (HNO_3) (veritas purity, GFS Chemicals). 0.10 g of this solution was then added to 2 wt% HNO_3 solution. A five point calibration curve was built using the following ICP standard solutions: 1,000 ppm Co in 2 wt% HNO_3, 1,000 ppm Al in 2 wt% HNO_3, 1,000 ppm Na in 2 wt% HNO_3, and 1,000 ppm Si in 2 wt% HNO_3. All standard solutions were purchased from Sigma-Aldrich (TraceCERT).

UV−visible spectroscopy (UV−vis) was used to determine the oxidation state of Co^{2+} ions and to detect the presence of cobalt oxides on Co-exchanged zeolites. Diffuse reflectance UV−vis spectra were recorded under ambient conditions using a Varian Cary 5000 UV−vis−NIR Spectrophotometer attached with a Harrick Scientific Praying Mantis diffuse reflectance

accessory. Barium sulfate ($BaSO_4$; 98 wt %, Sigma-Aldrich) was used to record the baseline spectra for every sample. Spectra were recorded from 10 000 to 50 000 cm^{-1} at a scan rate of 167 cm^{-1} s^{-1}. Typically, 0.10−0.15 g of Co-exchanged zeolite samples were loaded into a sample cup and pressed with a clean slide glass until the surface became flat.

4- MTO reaction

The H-form of the entire catalysts was obtained by ion exchange of calcined sample with 2.5 M NH_4Cl solution (80 °C and liquid to solid ratio of 10) for 2 hours. Finally, the NH_4-exchanged material was calcined at 500 °C for three hours in air.

The H-form of the catalysts was pelletized, crushed and sieved into 0.2-0.4 mm particle size. 50 mg of sample was mixed with 2 g quartz (Fluka) before being introduced into the fixed-bed reactor (7 mm diameter). N_2 (30 mL/min) was bubbled in methanol held at -17 °C, giving a WHSV = 0.8 h^{-1}. The catalyst was first activated with a nitrogen flow of 80 ml/min for 1 h at 540 °C, and then the temperature was decreased to reaction conditions (350 °C). Each experiment was analyzed every 5 min with an online gas chromatograph (Bruker 450GC, with PONA and Al_2O_3-Plot capillary columns, and two FID detectors). Conversion and selectivity were considered in carbon basis.

Supplementary Tables

Table S1. Elemental analyses of the as-prepared zeolites.

Sample	C (wt%)	N (wt%)	C/N (mol/mol)
AEI (OSDA **3**)	8.56	4.41	2.3
CHA (OSDA **12**)	13.53	1.50	10.4
CHA/**AEI** (OSDA **14**)	11.82	1.71	8.2

Table S2. Physico-chemical properties of the small-pore zeolites synthesized in this work.

Sample	Si/Al	Na/Al	BET surface area (m^2/g)	Micropore area (m^2/g)	External surface area (cm^3/g)	Micropore volume (cm^3/g)
AEI (std)	8.7	0.27	493	490	3	0.24
AEI (OSDA **3**)	9.7	0.25	496	493	3	0.24
CHA (std)	9.1	0.38	617	615	2	0.29
CHA (OSDA **12**)	9.2	0.34	602	597	5	0.29
CHA/**AEI** (OSDA **14**)	11.0	0.37	607	584	23	0.28

Table S3. Catalytic properties of the different small-pore zeolites for the MTO reaction (reaction conditions: T=350 °C, WHSV=0.8 h^{-1}, w_{cat}=50 mg; X_{95} is the methanol conversion drop below 95%).

		Selectivity (%) at X_{95}			**Olefin ratios at X_{95}**	
Sample	**Lifetime at X_{95} (min)**	**$C_2^=$**	**$C_3^=$**	**$C_4^=$**	**$C_3^=/C_2^=$**	**$C_4^=/C_2^=$**
AEI (std)	267	20.9	44.4	19.6	2.12	0.94
AEI (OSDA **3**)	490	23.1	48.5	22.1	2.08	0.94
CHA (std)	550	46.2	37.8	12.5	0.81	0.27
CHA (OSDA **12**)	781	47.8	36.0	11.4	0.75	0.24
CHA/**AEI** (OSDA **14**)	788	39.8	42.6	15.7	1.10	0.40

Supplementary Figures

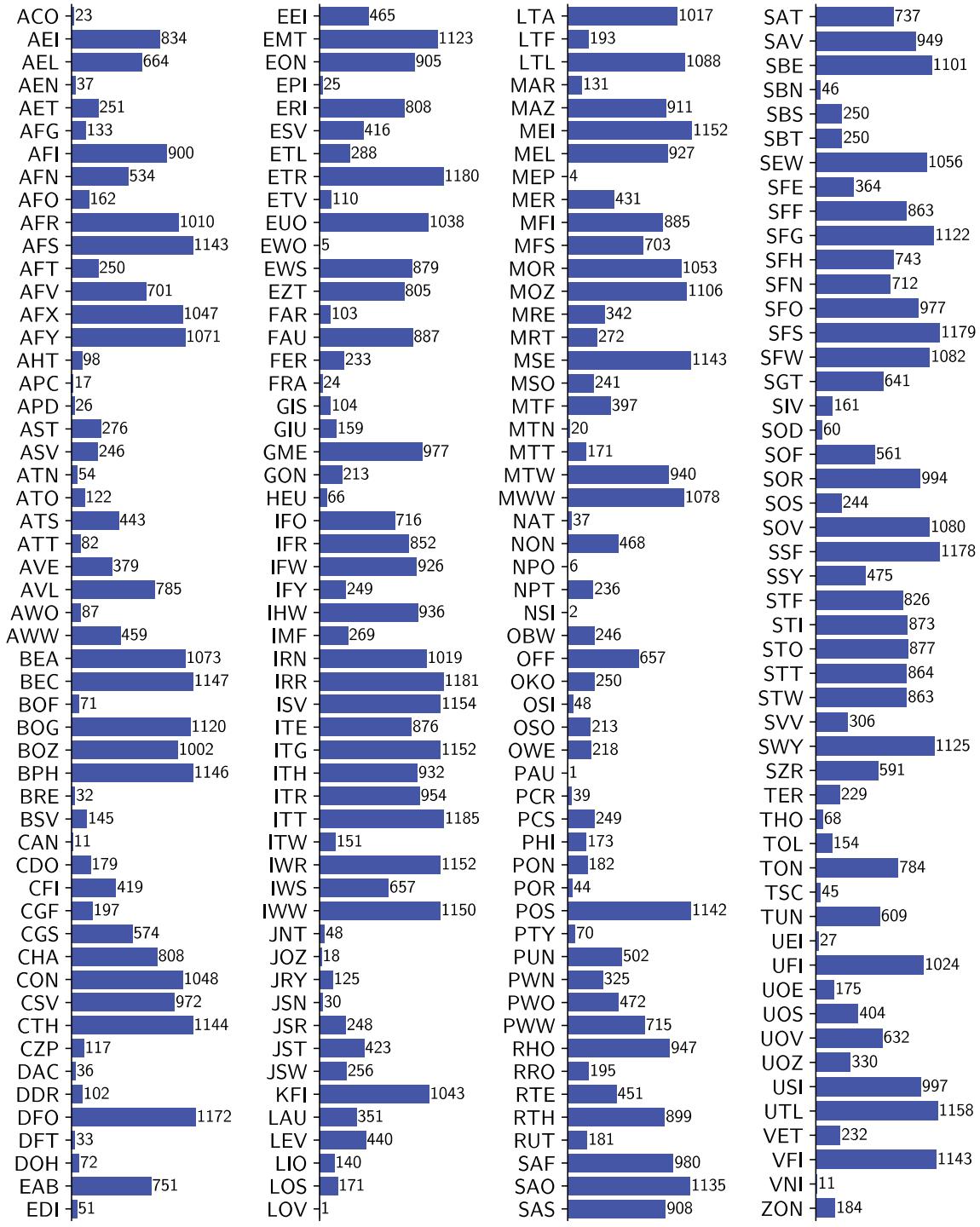

Figure S1: Number of distinct complexes for each of the 209 zeolite frameworks considered in this work.

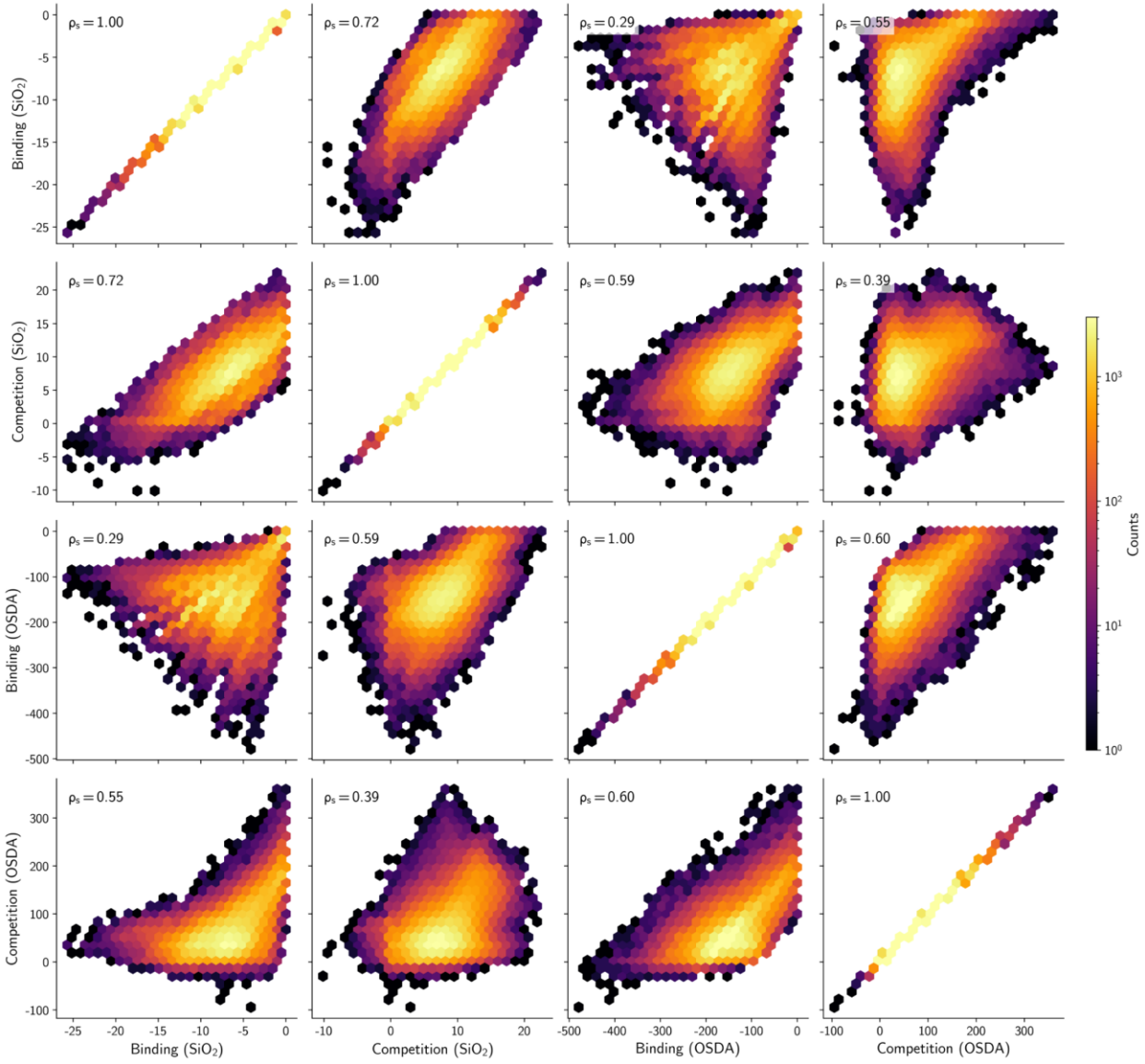

Figure S2: Correlation between binding energy metrics for all zeolite-OSDA pairs calculated in this work. Energies are given in kJ/mol SiO_2 and kJ/mol OSDA, depending on the normalization. ρ_s is the Spearman's rank correlation coefficient (*21*).

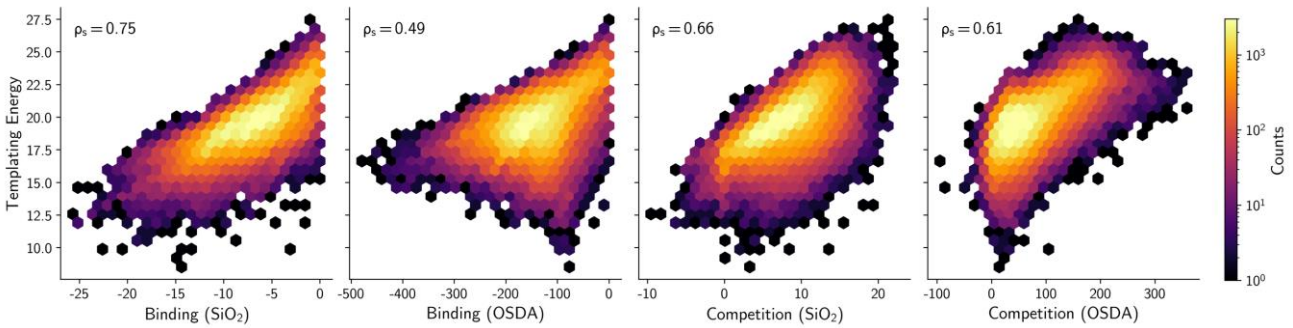

Figure S3: Correlation between the templating energy and the binding energy metrics in this work. The templating energy is given in kJ/mol and is calculated at 400 K. ρ_s is the Spearman's rank correlation coefficient (*21*).

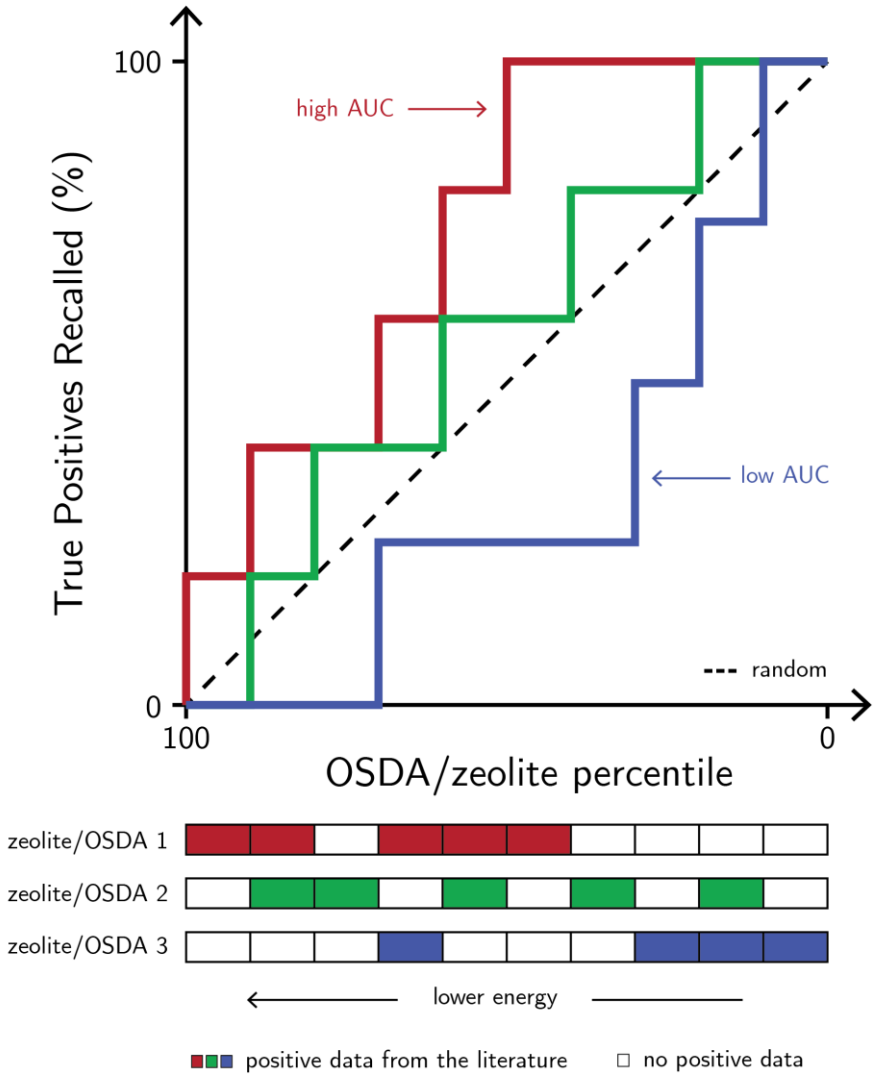

Figure S4: Diagram depicting the construction of the recall curve. The samples at the bottom are ordered according to an energy metric. Then, the cumulative number of true positives per sample is plotted against the percentile of each element.

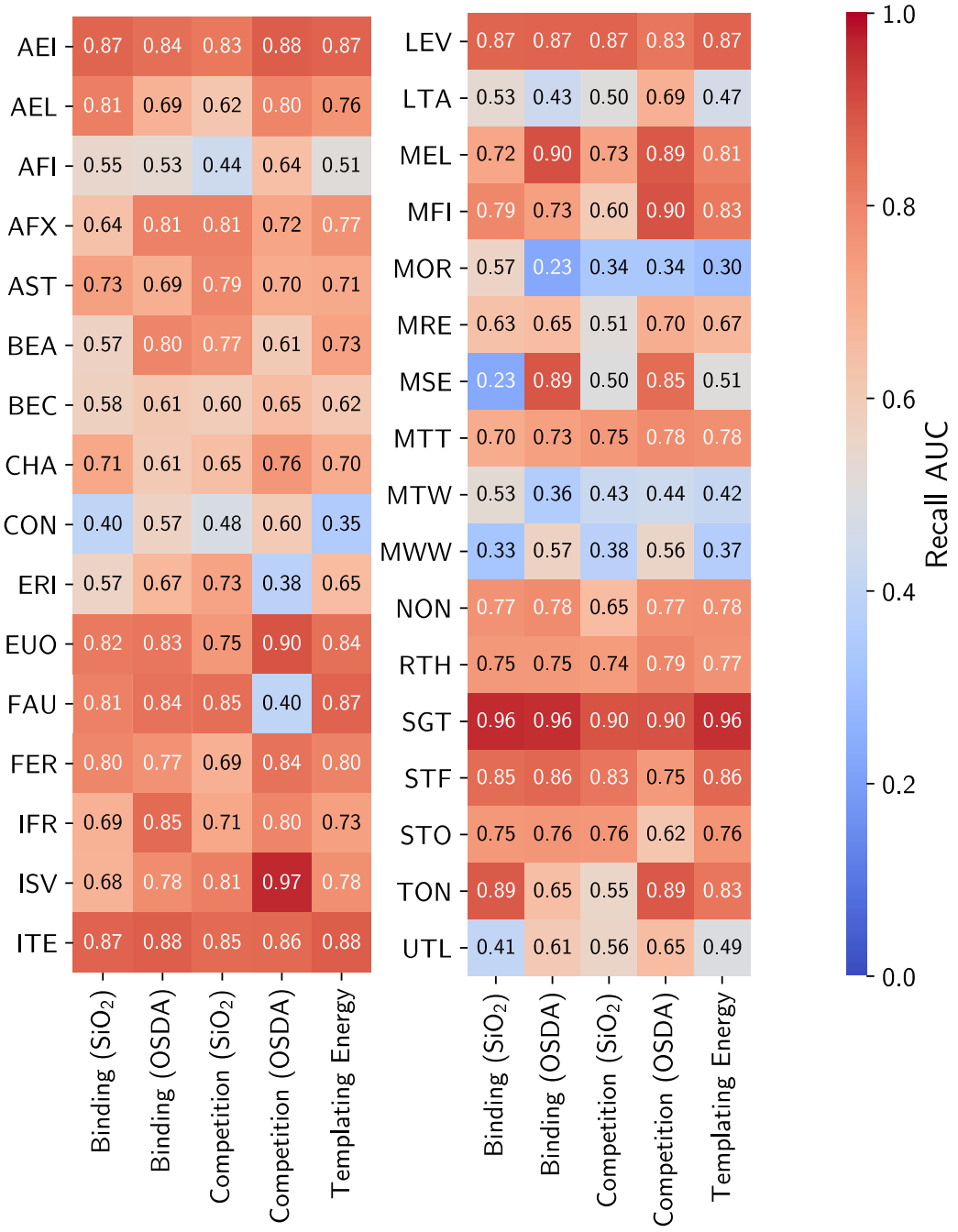

Figure S5: Recall AUC for the 33 zeolites with more than 10 different OSDAs in the literature. The AUC is calculated according to each of the five metrics explored in this paper.

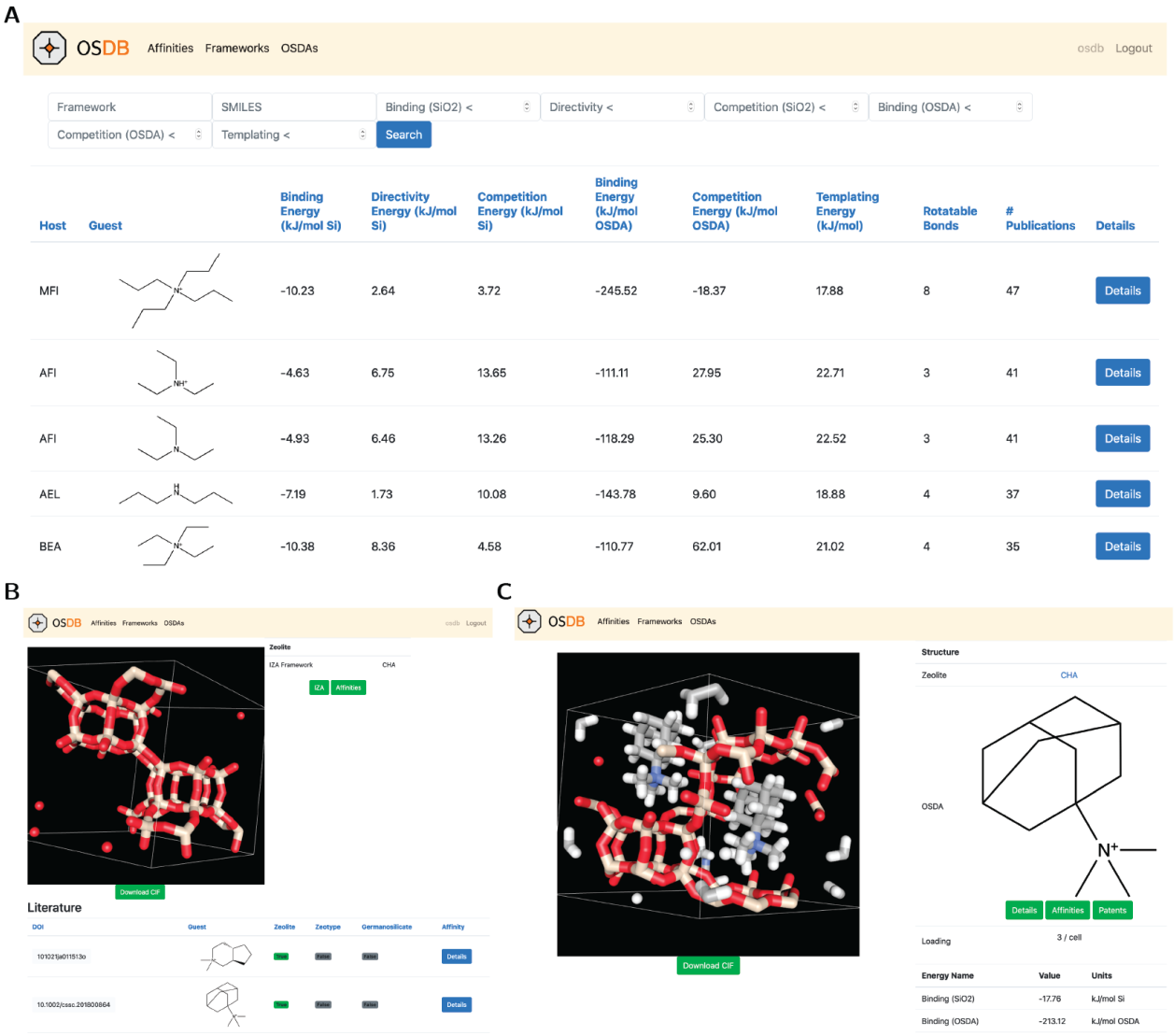

Figure S6: Visualization of the web interface to the database of calculations. OSDB enables researchers to (A) query and filter all OSDA-zeolite pairs in this article, (B) explore molecules and the literature of the frameworks, and (C) visualize each OSDA-zeolite pair and its metrics. Movie S1 shows features on the interactive search and rationalization of OSDAs for the frameworks.

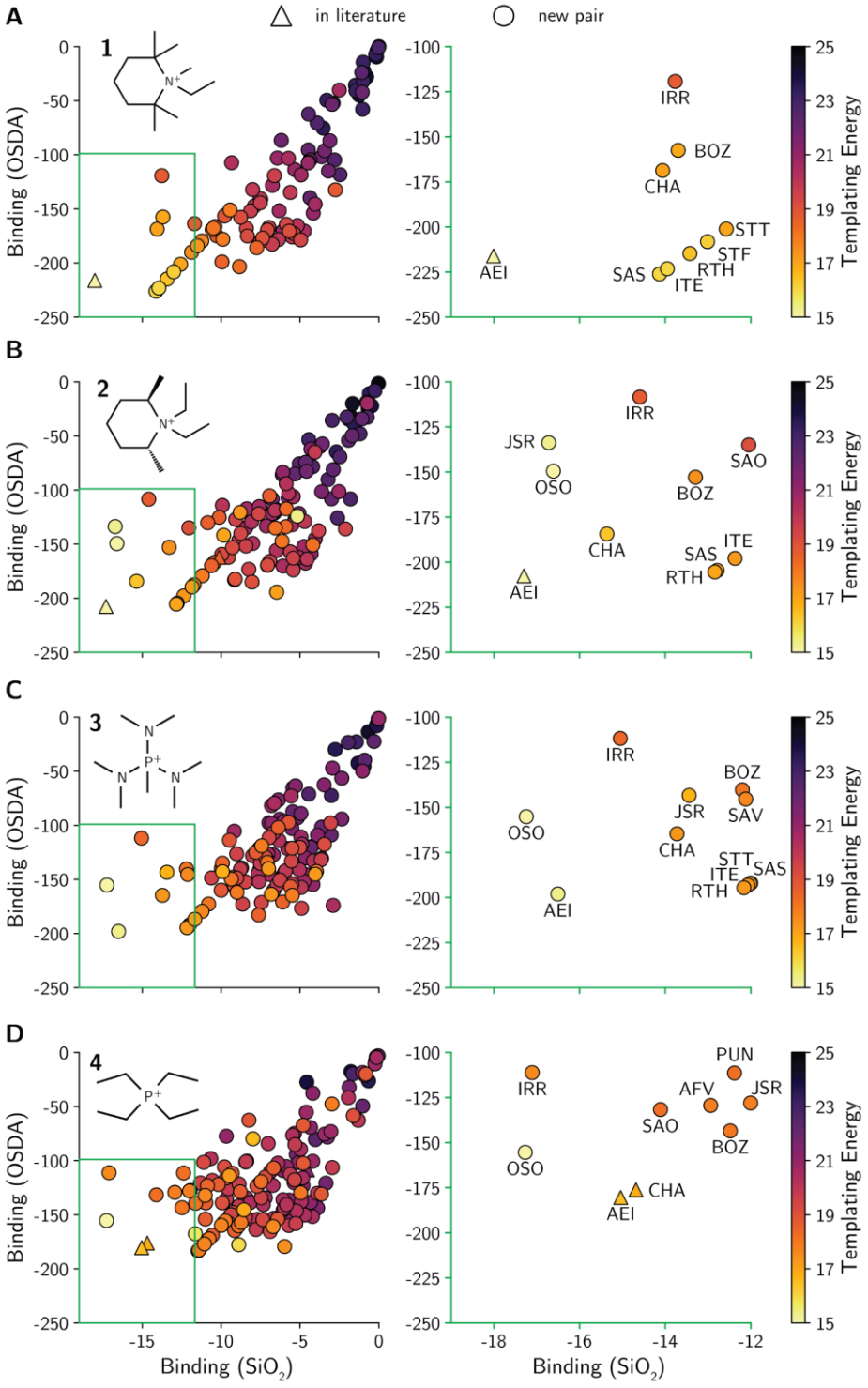

Figure S7: Phase competition for OSDAs **1**-**4**. The binding energy per OSDA (kJ/mol OSDA) and SiO_2 (kJ/mol SiO_2) are shown as independent parameters. The templating energy is given in kJ/mol. The green boxes on the left indicate regions expanded on the right column.Competing phases such as **OSO** or **IRR** may require different synthesis conditions (e.g., fluoride media and/or the inclusion of other heteroatoms, such as Be or Ge atoms) to be crystallized, and do not prevent the OSDAs from synthesizing the aluminosilicate **AEI**.

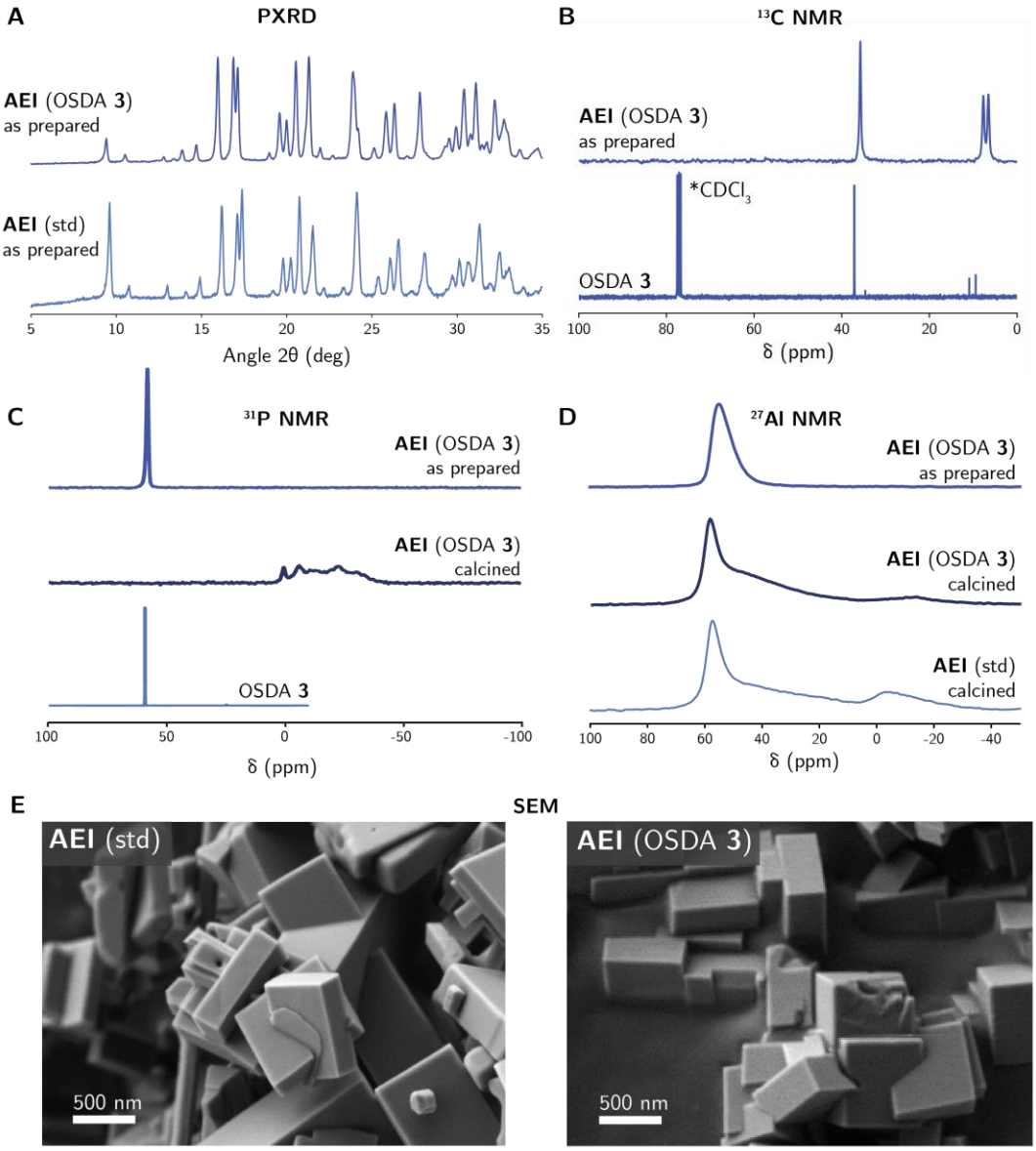

Figure S8: Characterization of the as-prepared **AEI** (OSDA **3**). (A) Powder X-ray diffraction (PXRD) shows the formation of the **AEI** phase. Elemental analyses coupled with (B) ^{13}C and (C) ^{31}P solid-state nuclear magnetic resonance (ssNMR) spectroscopy of the as-prepared **AEI** (OSDA **3**) sample reveal that OSDA **3** molecules remain intact within the **AEI** crystals after hydrothermal crystallization (see also Table S1). The Si/Al molar ratio of the **AEI** crystals was 9.7 (Table S2), and (D) the signal observed at ~52 ppm by ^{27}Al ssNMR spectroscopy indicates that Al species are in zeolite framework positions, even after the calcination. After the calcination treatment, ~1.6 wt% P (P/Al ~ 0.34) remained as extra-framework phosphate species, as shown in (C). N_2 adsorption measurements revealed a micropore volume of ~0.24 cm^3/g, in good agreement with standard SSZ-39 materials (Table S2) (*76*). Finally, (E) the formation of crystals with uniform particle sizes of ~500 nm is observed by scanning electron microscopy (SEM). In (A), (D) and (E), a comparison with **AEI** (std) is also shown.

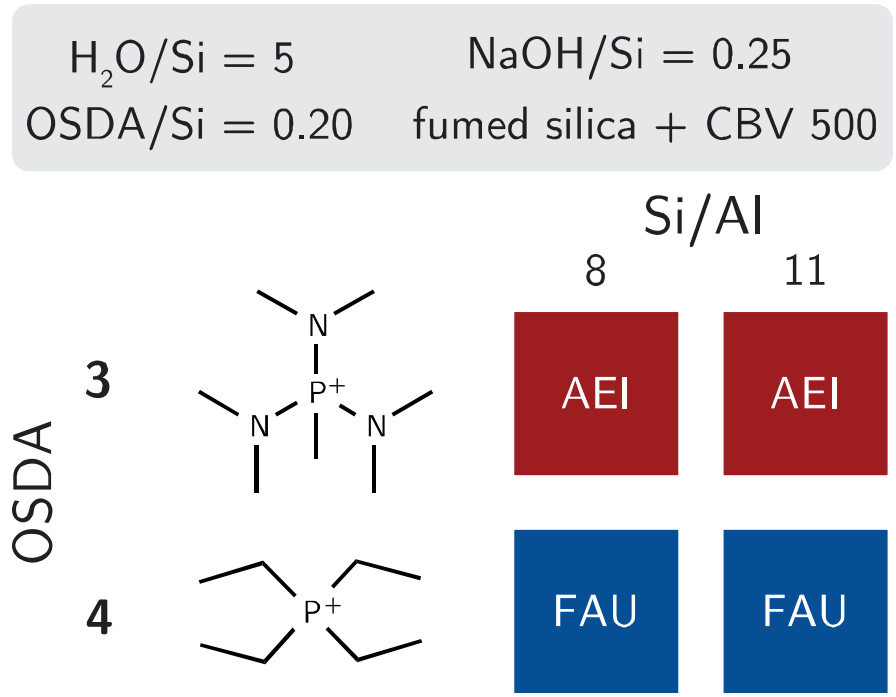

Figure S9: Synthesis outcomes for OSDAs **3** and **4** under demanding synthesis conditions. Fumed silica is used as Si source and CBV500 as Al source. The Si/Al ratio of the initial gel is 8 or 11, with $H_2O/Si = 5$, OSDA/Si = 0.20, and NaOH/Si = 0.25. In both these synthesis conditions, only OSDA **3** successfully crystallized **AEI** zeolite.

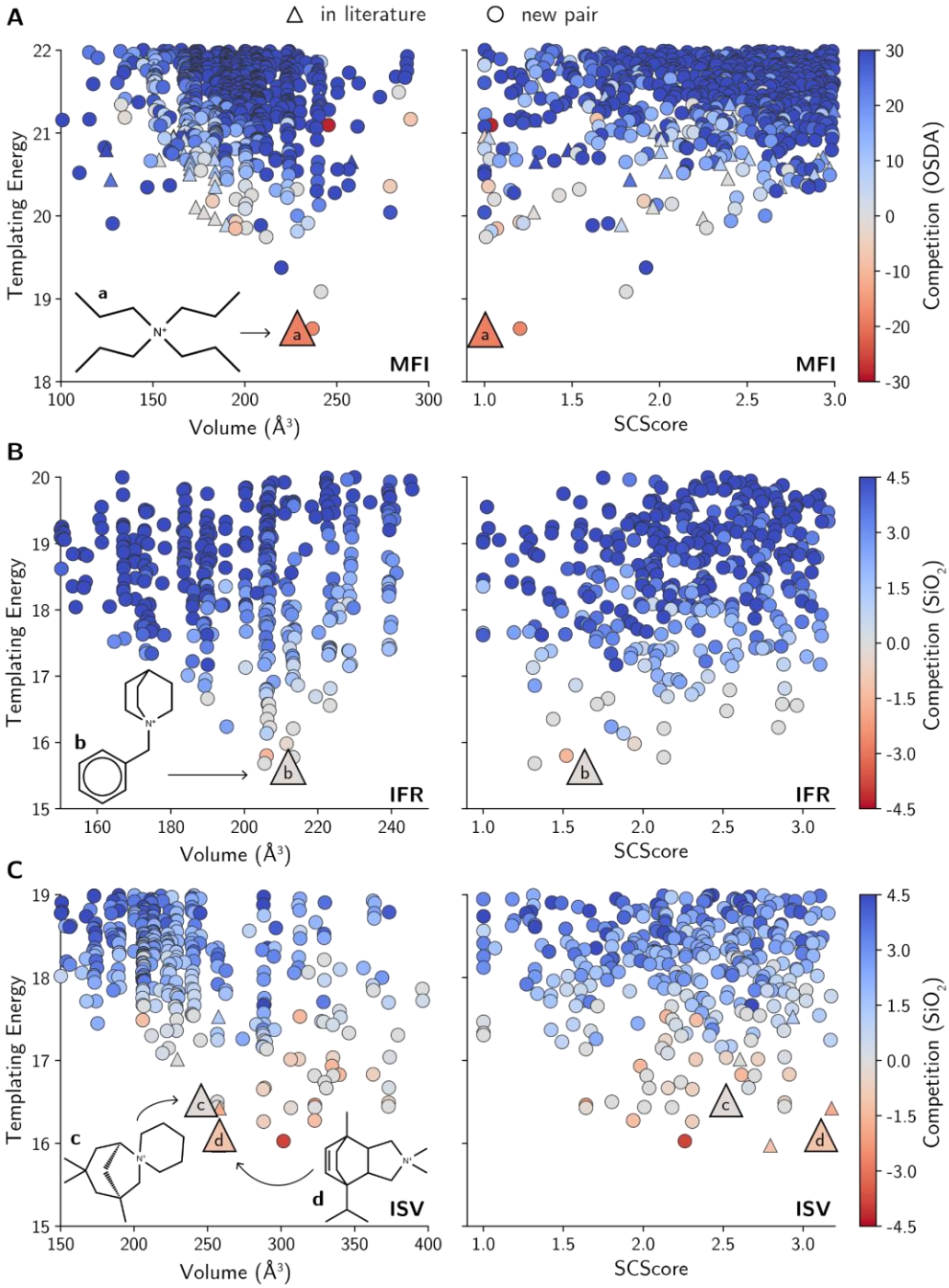

Figure S10: OSDA binding analysis for the (A) **MFI**, (B) **IFR**, and (C) **ISV** frameworks. The OSDAs used in the original discovery of these frameworks, such as tetrapropylammonium for **MFI** (OSDA **a**) (*77*), N-benzylquinuclidinium for **IFR** (OSDA **b**) (*78*), or 1,3,3-trimethyl-6-azoniumtricyclo[3.2.1.$4^{6,6}$]dodecane (OSDA **c**) (*79*) and 1-isopropyl-4,4,7-trimethyl-4-azonia-tricyclo[5.2.2.0] undecane-8-ene (OSDA **d**) (*7*) for **ISV** are highlighted among the best templates for these structures.

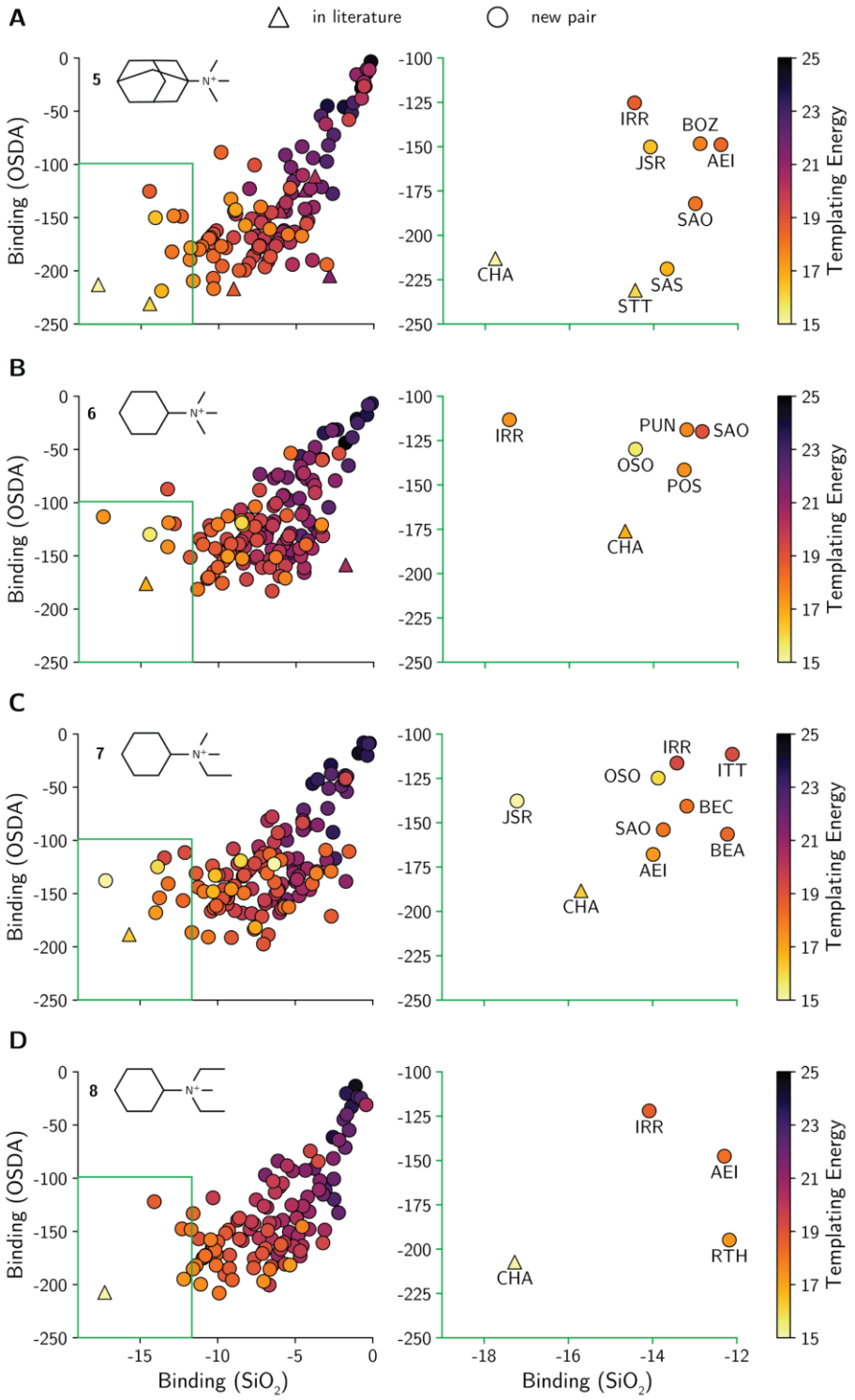

Figure S11: Phase competition for OSDAs **5-8**. The binding energy per OSDA (kJ/mol OSDA) and SiO_2 (kJ/mol SiO_2) are shown as independent parameters. The templating energy is given in kJ/mol. The green boxes on the left indicate regions expanded on the right column.

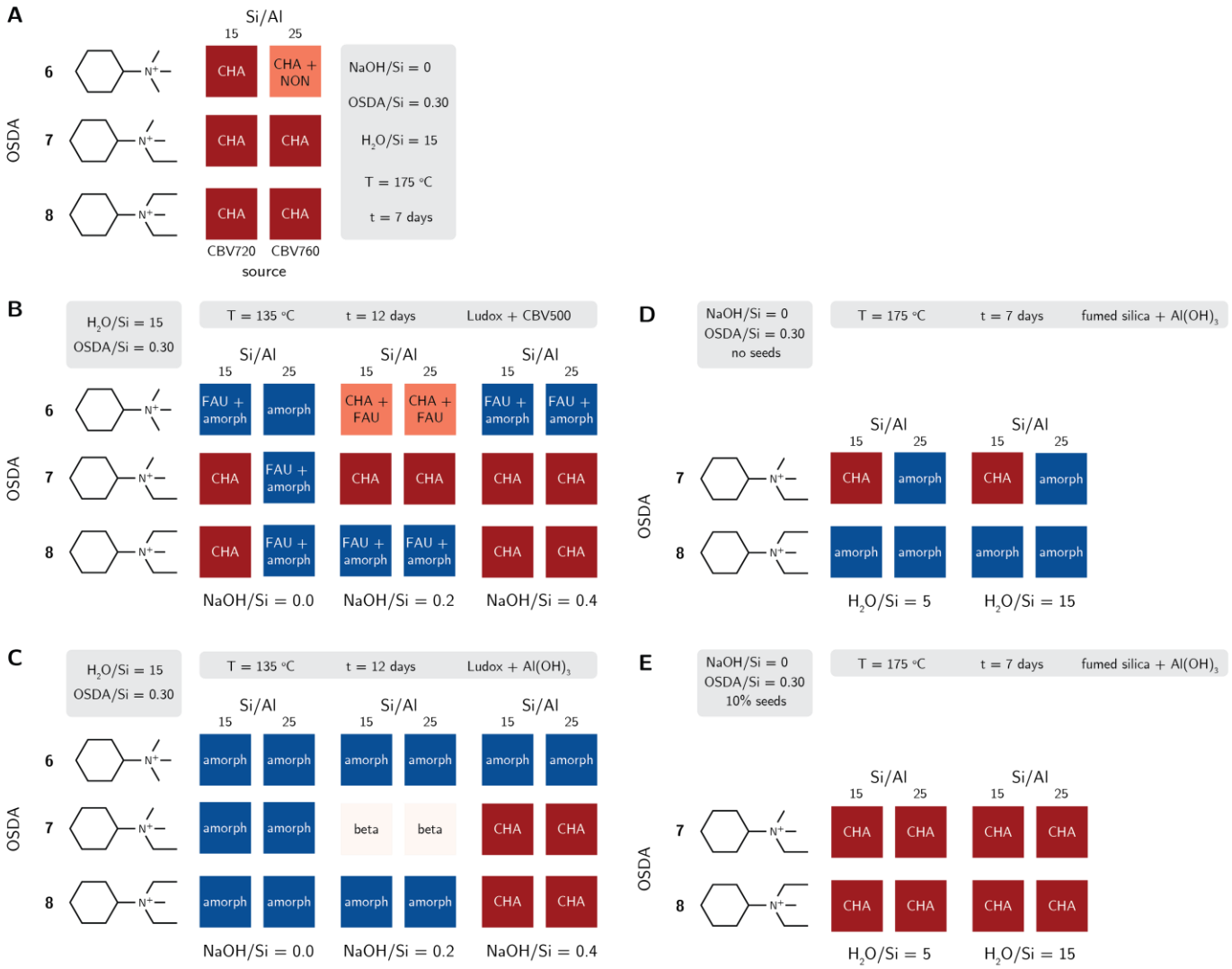

Figure S12: Synthesis outcomes from OSDAs **6-8** in a variety of synthesis conditions, including: (A) using CBV720 and CBV760 as Si/Al sources in Na-free media; using Ludox as Si source and (B) CBV500 or (C) $Al(OH)_3$ as Al source with or without Na; using fumed silica and $Al(OH)_3$ as Si and Al sources, respectively, in the (D) absence or (E) presence of seeds.

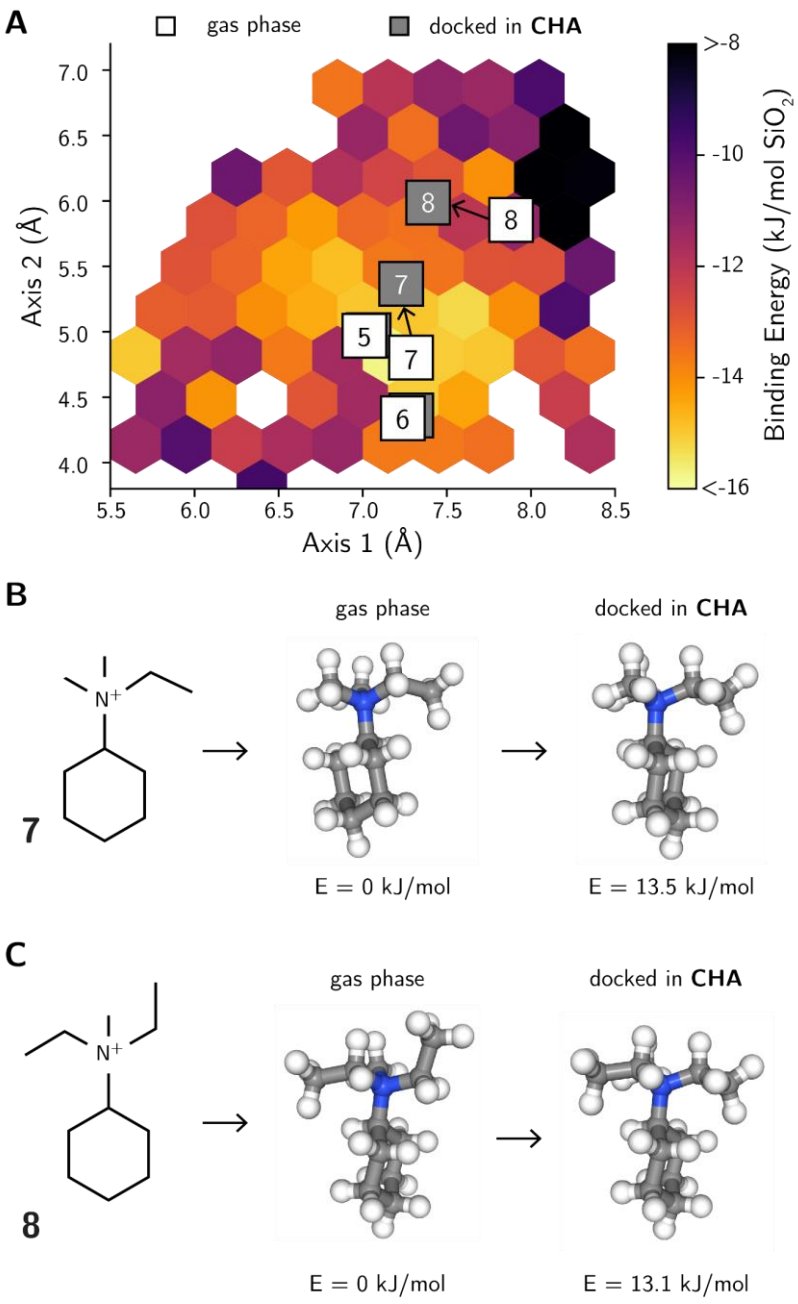

Figure S13: (A) Differences between the shapes of OSDAs **5-8** in the gas phase and occluded in the cha cavity. Although OSDAs **5** and **6** do not undergo significant distortions to fit in the cha cage, OSDAs (B) **7** and (C) **8** have to change their shape, increasing the energy of the docked conformer. Since the docked conformation for both OSDA **7** and **8** have similar energies above its gas phase geometry, the molecular distortion energies are insufficient to predict differences in templating abilities. Instead, the shape descriptors shown in (A) may complement binding energies in the prediction of phase selectivity in zeolite synthesis.

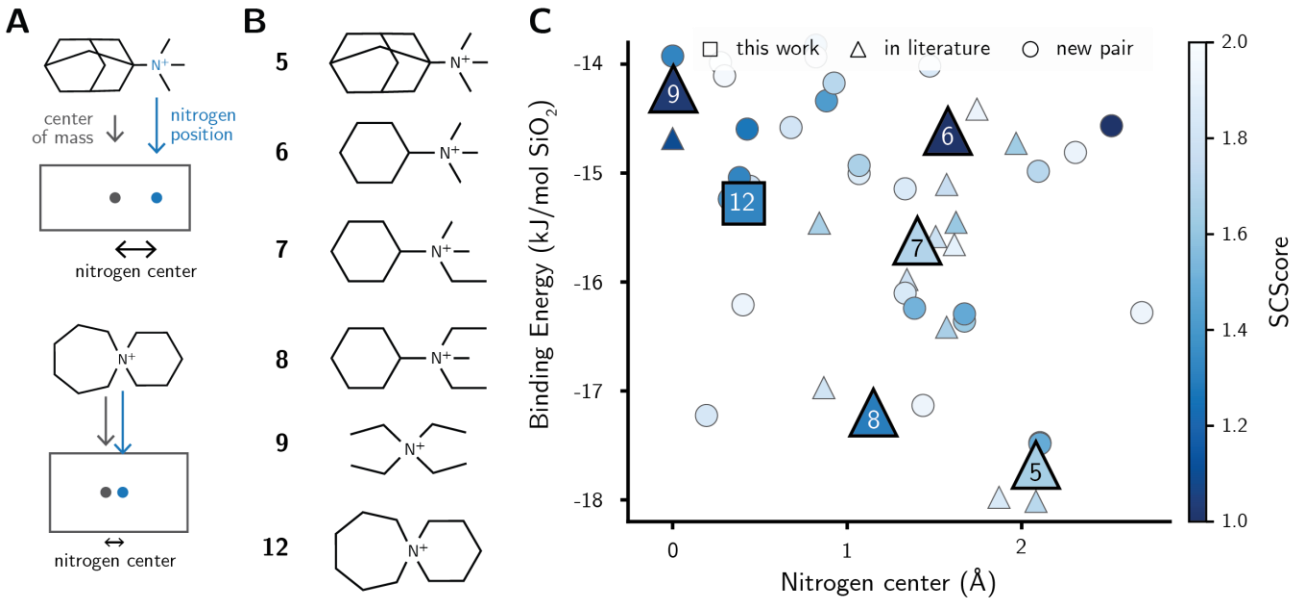

Figure S14: (A) Charge descriptor used to screen OSDAs for **CHA** with different charge distributions. The nitrogen center is taken as the distance between the nitrogen atom and the center of mass of the molecule. (B) Molecules with different nitrogen centers, as also shown in (C). This charge descriptor may be specific to the **CHA** cage, and further extensions of this analysis may be required for predicting charge distributions of more complex OSDAs and their biasing ability towards other zeolites.

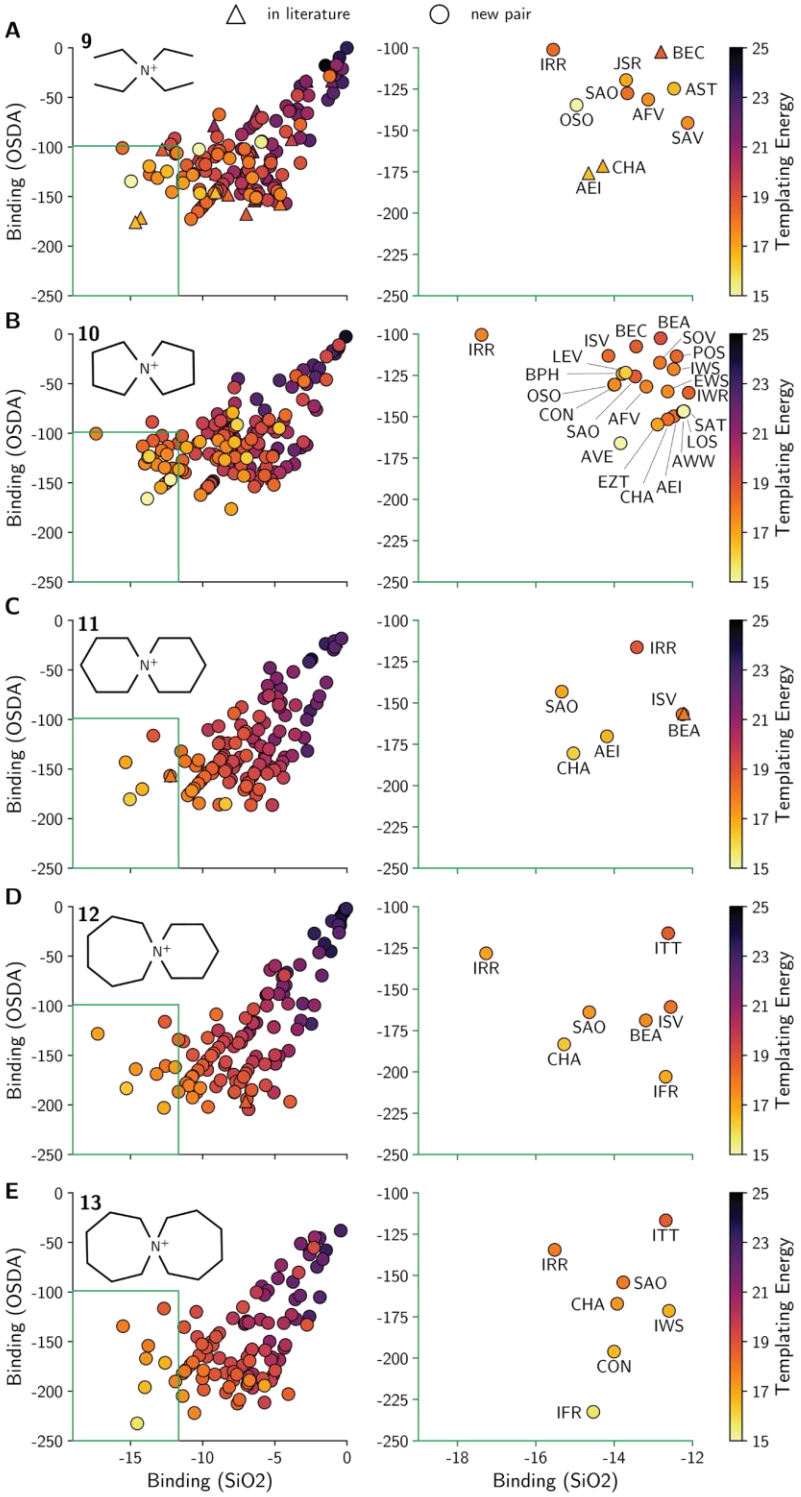

Figure S15: Phase competition for OSDAs **9-13.** The binding energy per OSDA (kJ/mol OSDA) and SiO_2 (kJ/mol SiO_2) are shown as independent parameters. The templating energy is given in kJ/mol. The green box on the left column indicates the region expanded on the right column. A favorable binding energy of OSDA **5** is found for **IRR** zeolite due to a pose with large loading for this extra-large pore zeolite.

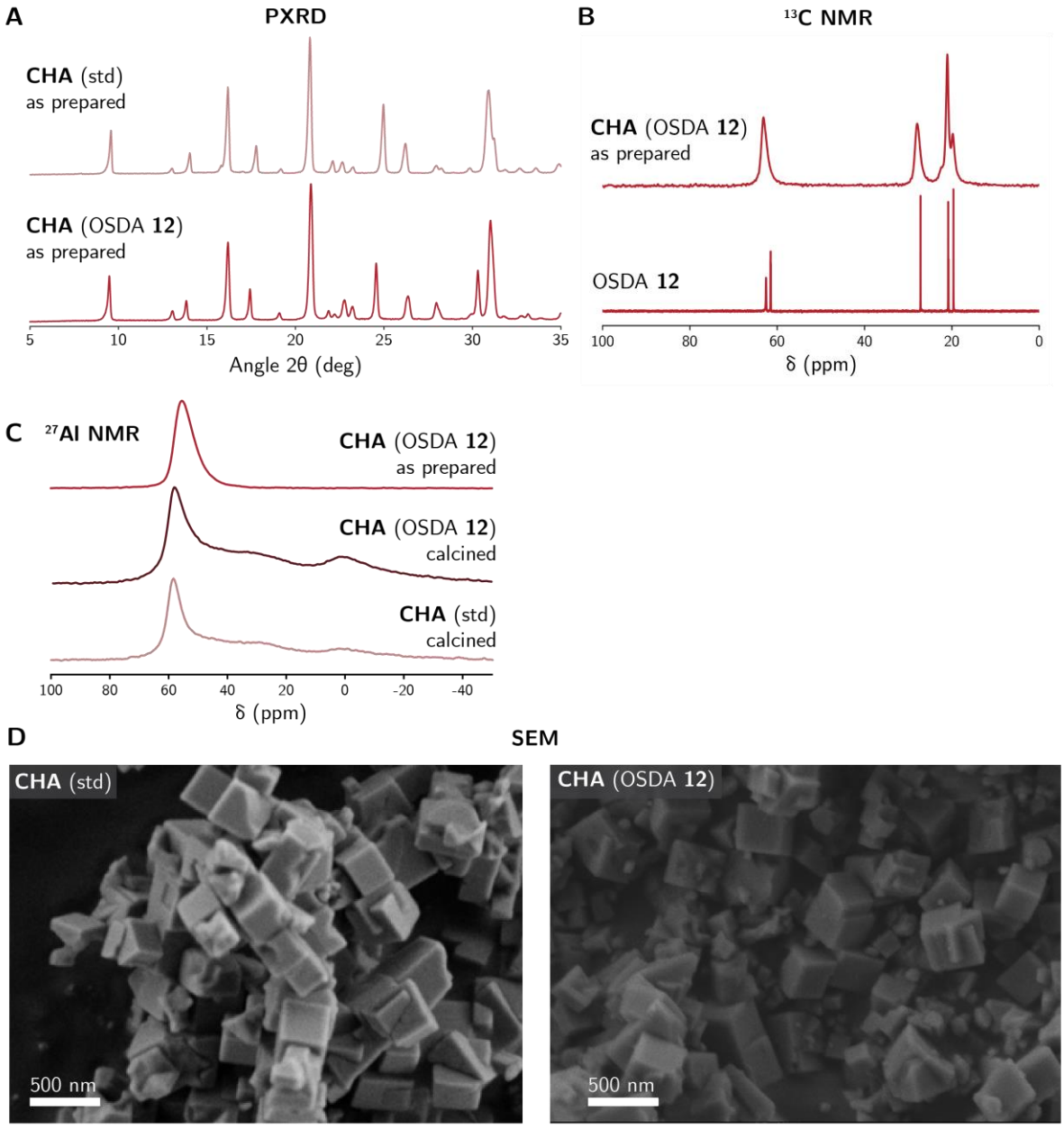

Figure S16: Characterization of the as-prepared **CHA** (OSDA **12**). PXRD confirms the crystallization of the pure **CHA** structure (A), with occluded OSDA **12** molecules kept intact after the hydrothermal synthesis (B, also Table S1). The sample featured a Si/Al molar ratio of 9.2 (Table S2), with (C) all Al species in tetrahedral coordination as confirmed by ^{27}Al ssNMR, even after the calcination. (D) The average particle size of the **CHA** crystals was found to be 200-300 nm, with a micropore volume of 0.29 cm^3/g after calcination (Table S2). In (A), (C), and (D), a comparison with **CHA** (std) is also shown.

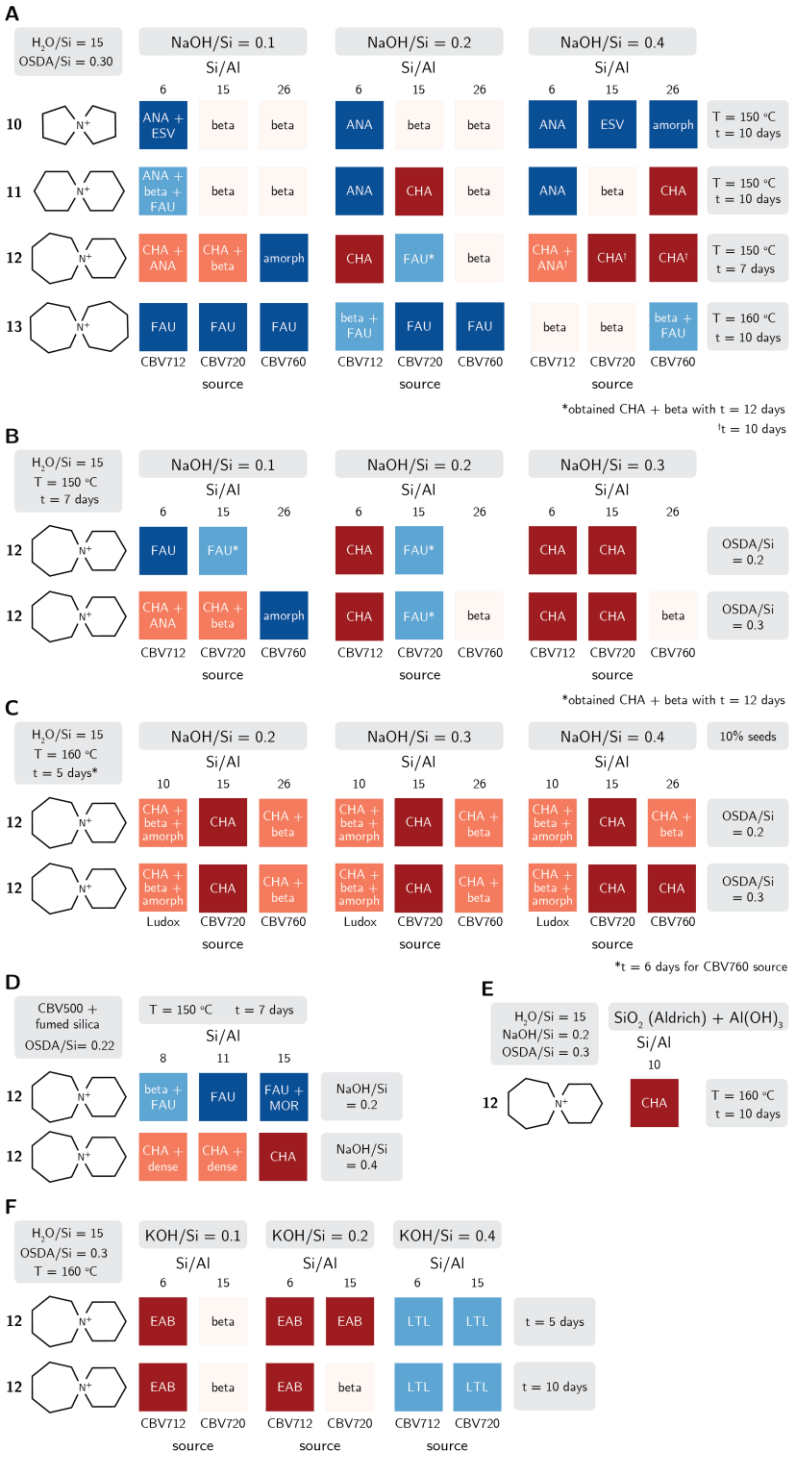

Figure S17: (A) Synthesis outcomes from OSDAs **10**-**13** in a variety of synthesis conditions using CBV712, CBV720, and CBV760 as Si and Al sources. Outcomes of syntheses experiments with OSDA **12** using: (B) smaller quantities of OSDAs and crystallization times; (C) seeds and different Si and Al sources; (D) fumed silica as Si source and CBV500 as Al source; (E) an amorphous Si source; and (F) potassium as inorganic structure-directing agent.

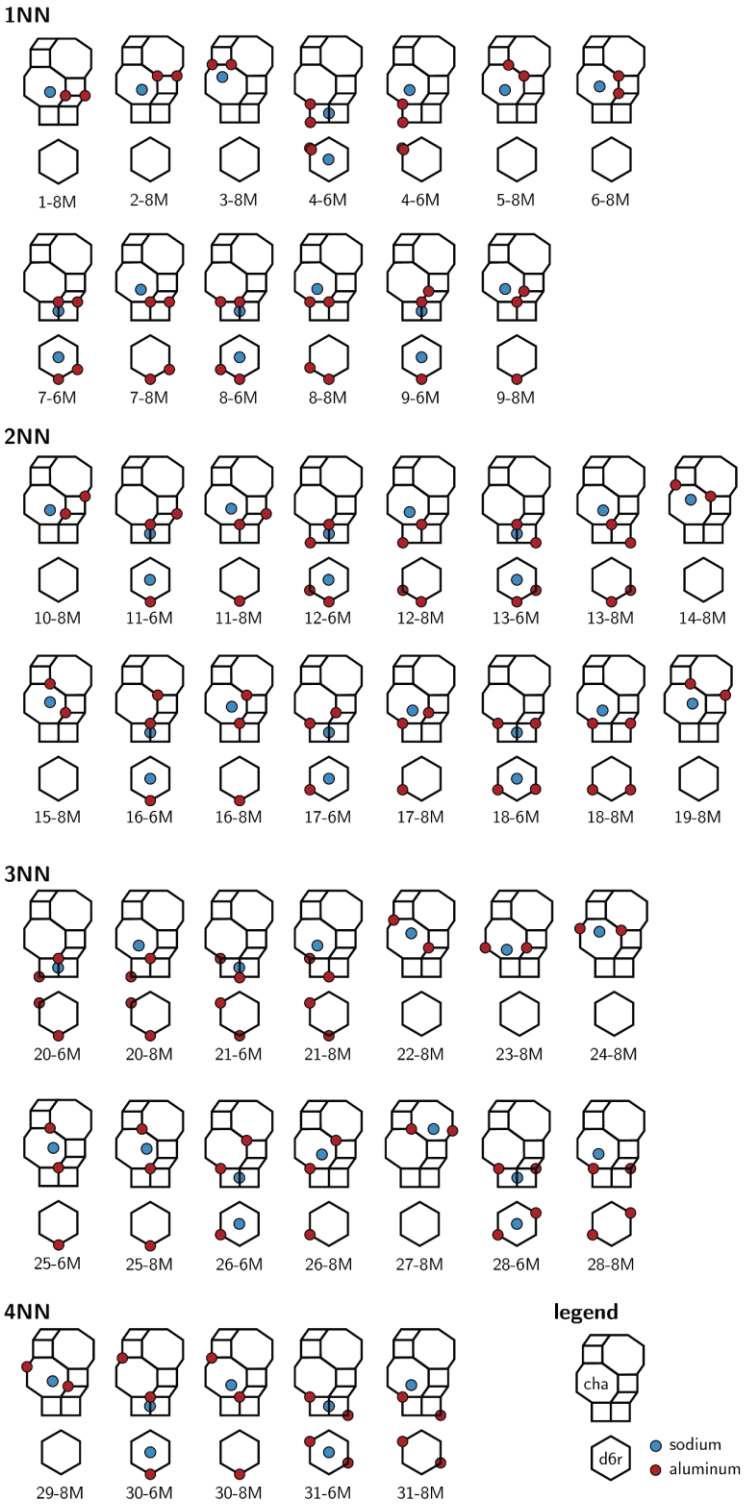

Figure S18: Aluminum and sodium distributions for the cha cage studied in this work, as proposed in (*43*). The IDs of the distributions are grouped by the graph distance between the aluminum pairs.

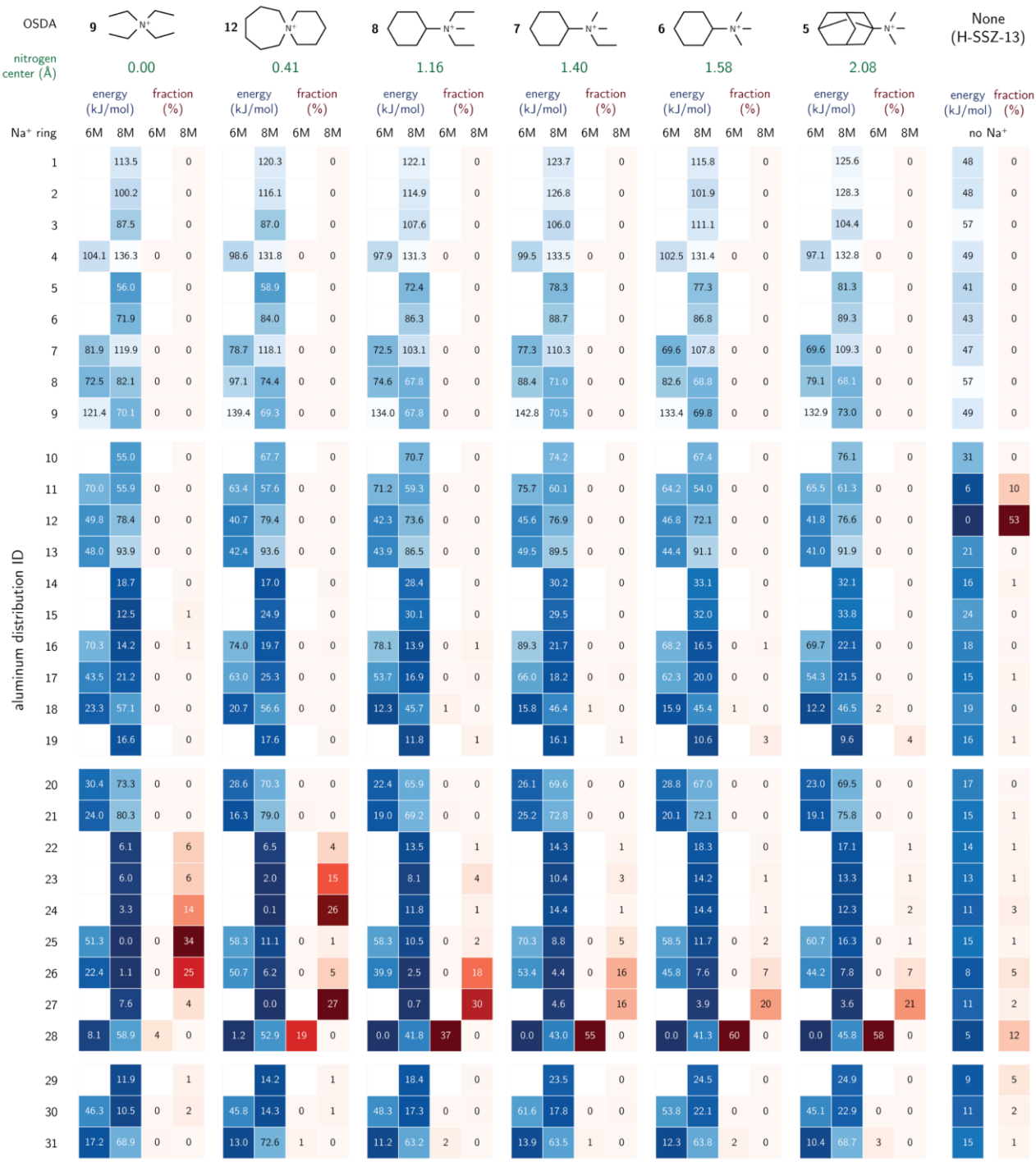

Figure S19: Influence of the OSDA on the relative energies (blue) and predicted fraction of aluminum pairs (red) for all aluminum distributions in the cha cage. The aluminum ID corresponds to the distribution shown in Fig. S18. The protonated form of **CHA** (i.e., without OSDAs or Na^+) is also calculated for comparison. The fraction of aluminum pairs is calculated at 433 K.

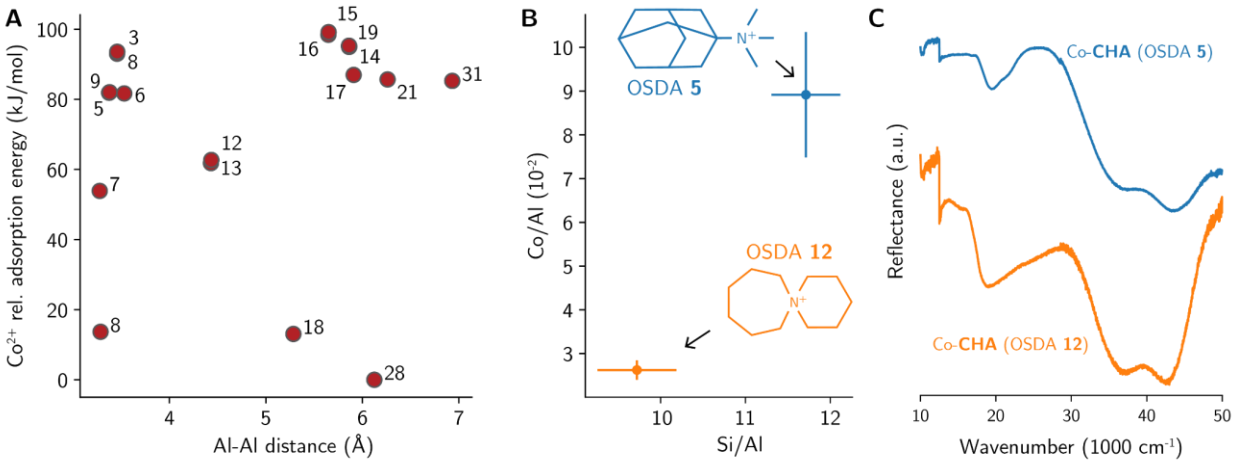

Figure S20: (A) DFT adsorption energies of Co^{2+} ions on cha cages with different aluminum distributions relative to the most stable configuration. The index of each point refers to the distribution ID shown in Fig. S17. Only distributions within 100 kJ/mol of the most stable configuration (ID 28) are displayed. The calculations indicate that the adsorption of Co^{2+} in d6r units with paired aluminum sites is the most favorable configuration, for which the Co-exchange is known to be favorable (*80*). The calculated energies are in quantitative agreement with previous studies (*43*). (B) Results of Co/Al and Si/Al measurements for several **CHA** samples synthesized with OSDAs **5** and **12**. The results indicate that **CHA** (OSDA **5**) samples have, 3.4 ± 0.8 more paired aluminum sites in d6r units (configuration 28) than **CHA** (OSDA **12**) samples, in agreement with the DFT predictions (see Fig. 3E and Fig. S19). Error bars are the standard error of the mean for 7 and 10 measurements for **CHA** samples synthesized with OSDAs **5** and **12**, respectively. (C) Drift UV-Vis spectra of Co-exchanged **CHA** zeolites synthesized with OSDAs **5** and **12**. No absorption peak was observed between 25,000 and 32,000 cm^{-1}, implying no cobalt oxide was formed during ion-exchange and calcination process. Instead, all cobalt atoms are expected to be coordinated to paired aluminum sites.

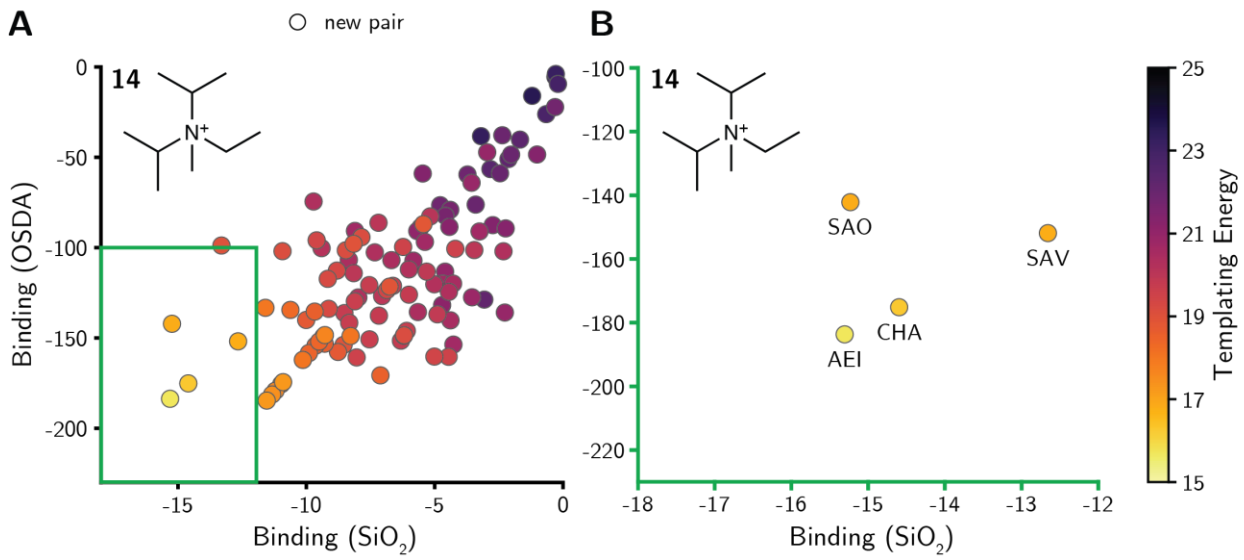

Figure S21: phase competition for OSDA **14**. The binding energy per OSDA (kJ/mol OSDA) and SiO_2 (kJ/mol SiO_2) are shown as independent parameters. The templating energy is given in kJ/mol. The green box in (A**)** indicates the region expanded in (B).

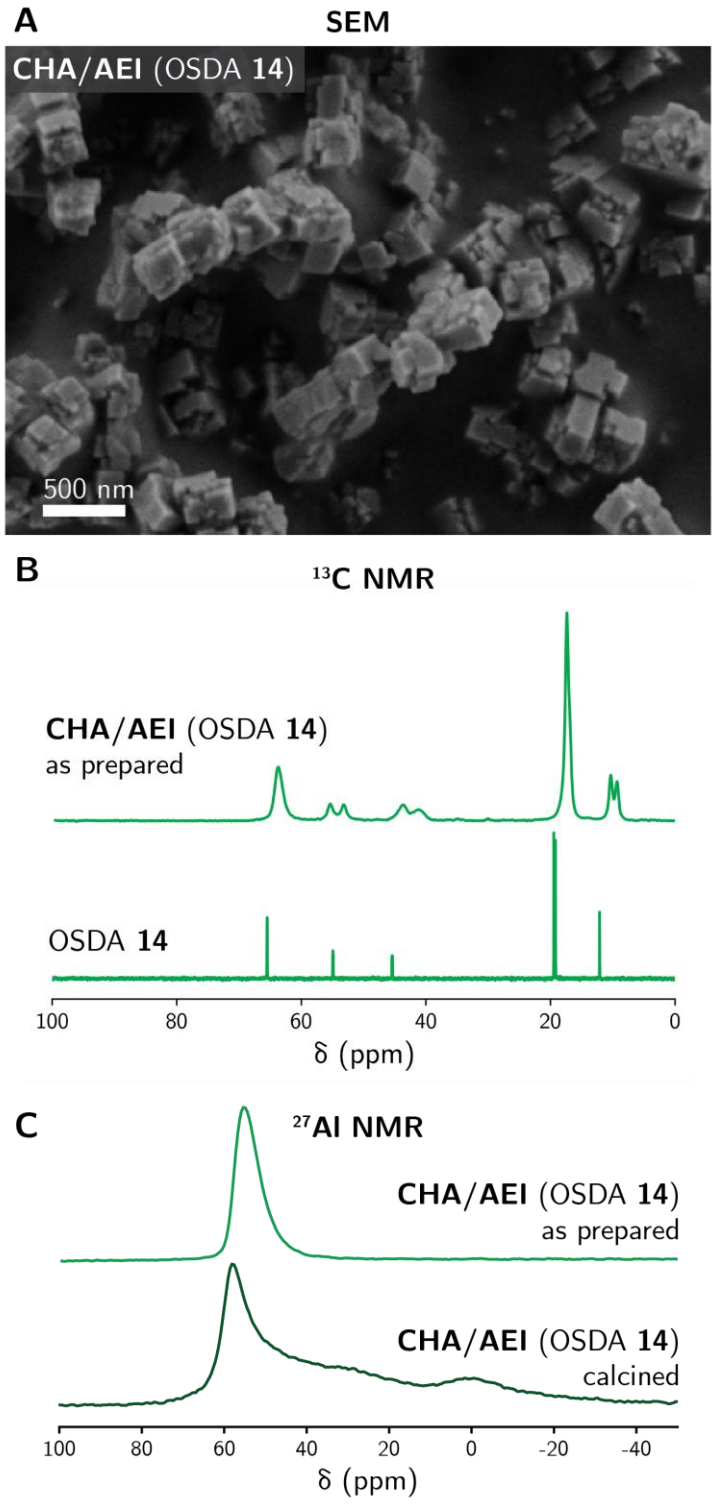

Figure S22: Characterization of the as-prepared **CHA/AEI** (OSDA **14**) with (A) SEM, (B) ^{13}C NMR, and (C) ^{27}Al NMR. The calcined **CHA/AEI** (OSDA **14**) ^{27}Al NMR spectrum is also shown in (C).

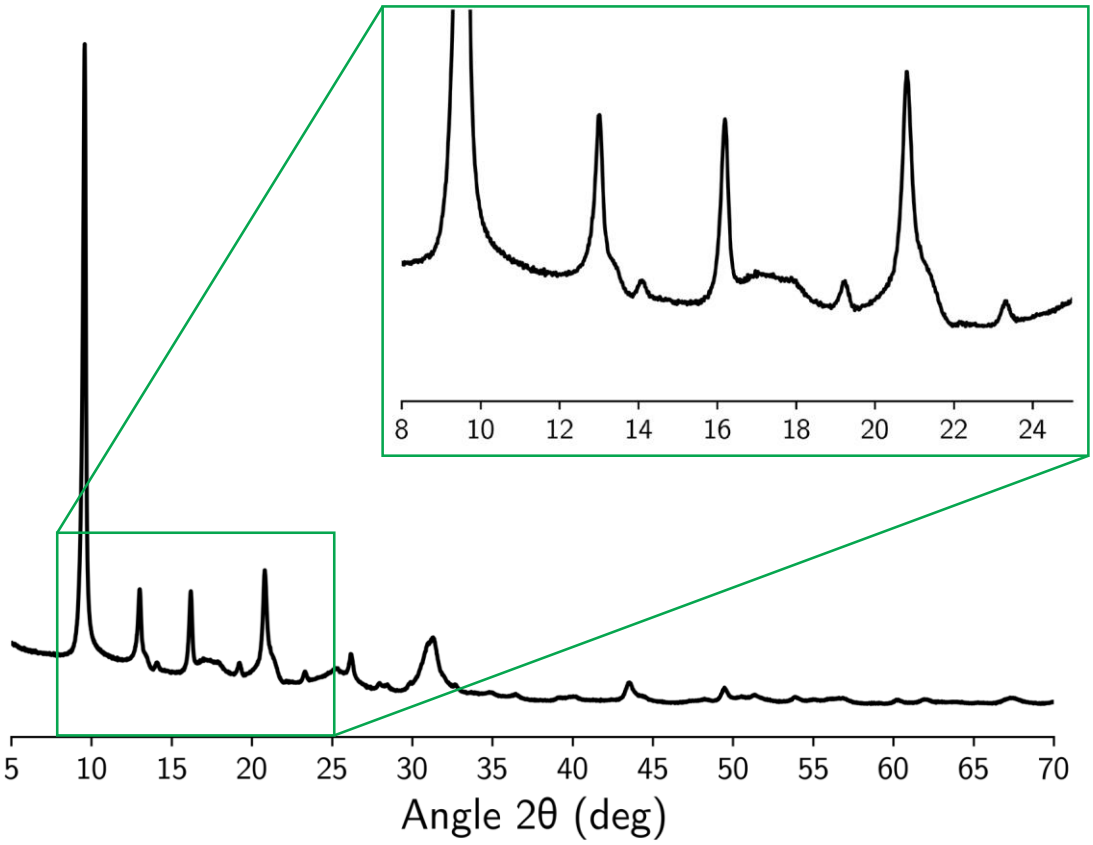

Figure S23: Experimental PXRD pattern of the calcined **CHA/AEI** (OSDA **14**) sample.

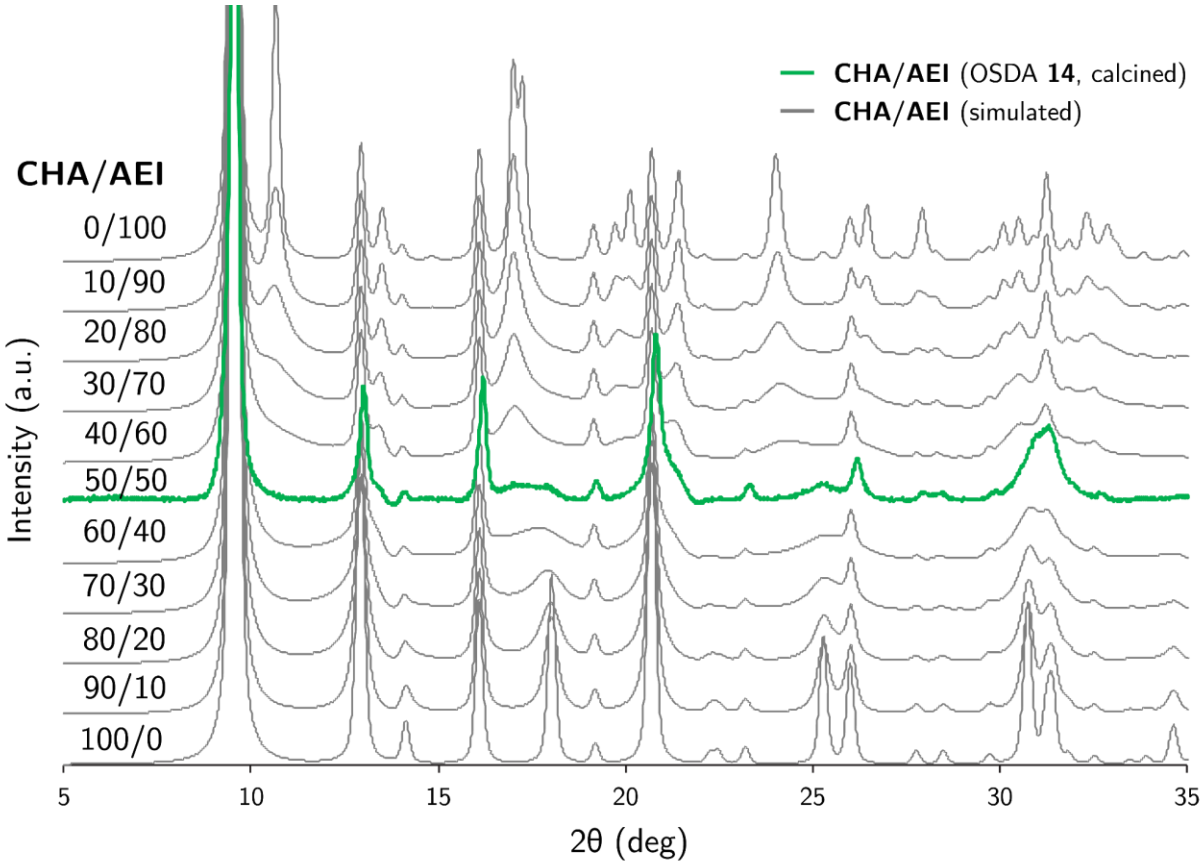

Figure S24: Experimental PXRD pattern of the calcined **CHA/AEI** (OSDA **14**) sample (green) superimposed with simulated patterns of randomly intergrown phases with different **CHA/AEI** content (gray). Simulation performed using DIFFaX.

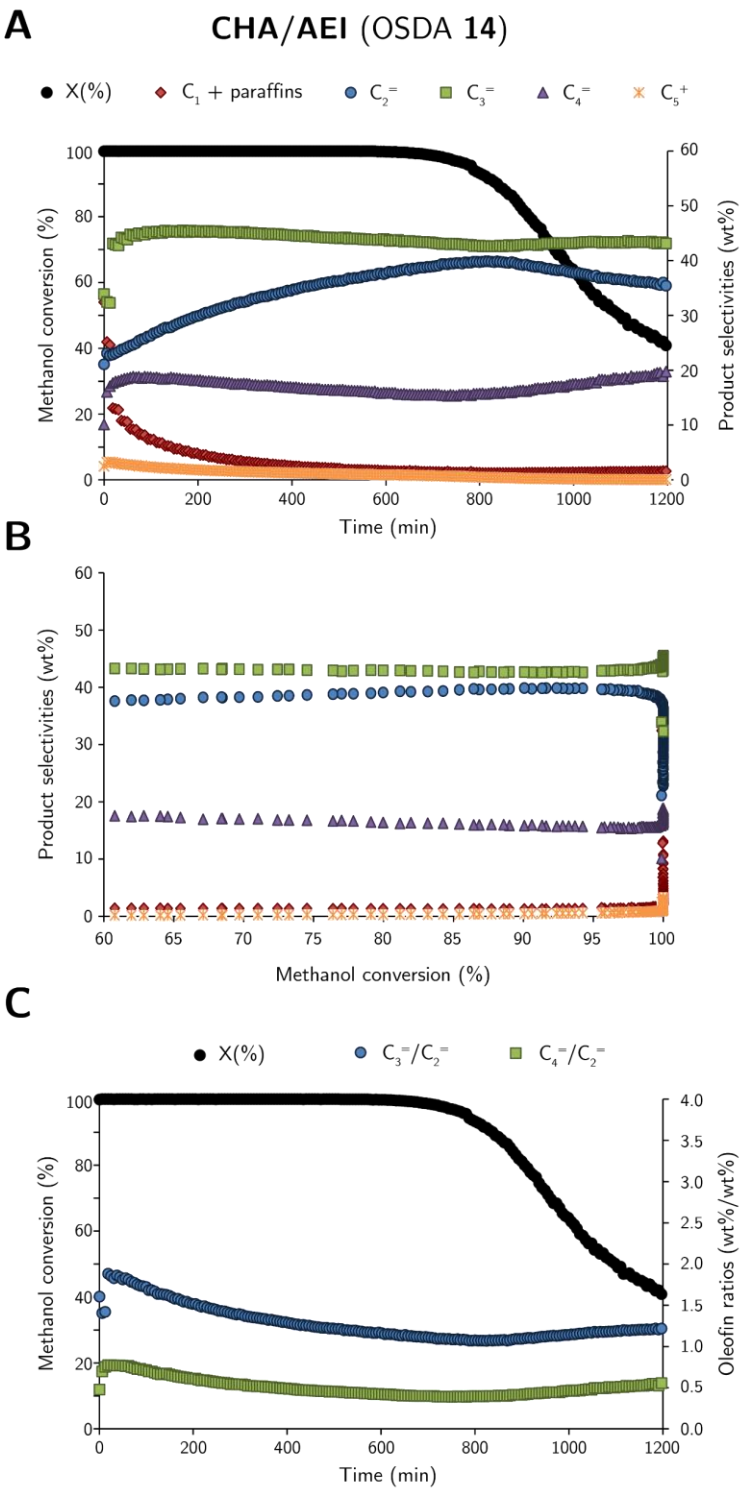

Figure S25: MTO performance using **CHA/AEI** (OSDA **14**). (A), Methanol conversion and product selectivity with TOS; (B), Product selectivity versus conversion; (C) methanol conversion, $C_3^=/C_2^=$ and $C_4^=/C_2^=$ vs TOS. Reaction conditions: T = 623 K, WHSV = 0.8 h^{-1}, w_{cat} = 50 mg.